Università degli studi di Bologna

Facoltà di Scienze Matematiche Fisiche e Naturali

Dottorato di Ricerca in Fisica

XIX ciclo

Algorithms for the analysis of neutrino interactions in the OPERA-like Emulsion Cloud Chambers

Author: **Lucia Consiglio**

Advisors:

Prof. Giorgio Giacomelli

Dott. Gianni Mandrioli

Prof. Ettore Remiddi

PhD Coordinator:

Prof. Fabio Ortolani

Bologna,15 Marzo 2007

Contents

Introduction

The Standard Model (SM) of Particle Physics, which includes electroweak and strong interactions, has been tested very precisely, in particular at the LEP collider. In this theory, the neutrinos are masseless particles; but there is a growing experimental evidence for neutrino oscillations, which imply neutrinos with non vanishing masses and physics beyond the SM.

The neutrino oscillations hypothesis was first proposed by Bruno Pontecorvo in 1958 in the form of neutrino-antineutrino oscillations. After the discovery of other neutrinos, the idea was extended to oscillations among different flavors.

The first indication of neutrino oscillations came in the 70s from the observation of a deficit of the solar neutrino flux measured on Earth. Other indications came from atmospheric neutrinos in the 80s. More recent experimental results have contributed to reinforce the evidence of the atmospheric neutrino anomaly. The favoured explanation of this phenomenon is $\nu_\nu \rightarrow \nu_\tau$ oscillations. This implies that neutrinos have non vanishing masses and that their flavor eigenstates involved in weak interaction processes are a superpositions of mass eigenstates. All experiments performed up to now, are disappearance experiments, and thus one doesn't have a final proof of the $\nu_\nu \rightarrow \nu_\tau$ appearance oscillation.

This is one of the main goals of the OPERA experiment, in preparation at Gran Sasso, which uses the long baseline (L $\sim$730 km) CNGS neutrino beam produced at CERN. Since the ν_e contamination in the CNGS beam is low, OPERA will also be able to search for the subdominant $\nu_\mu \rightarrow \nu_e$ oscillation channel.

OPERA is a large scale "hybrid" detector made of 2 supermodules. Each one

is equipped with electronic detectors, an iron spectrometer and a $\sim$0.9 kton target section made of Emulsion Cloud Chambers units with nuclear emulsions and lead absorbers. The production and the decay of the τ lepton is observed thanks to the excellent position resolution of nuclear emulsions. The use of a Pb-emulsion target satisfies the need of a large mass and of the high tracking capability to detect τ decays. The electronic detectors of OPERA localize the position of the brick where the neutrino interaction occurred. The candidate brick is then extracted, the emulsions are processed and then scanned with fast automatic microscopes.

The main aim of this thesis concerns the study of the algorithms for the reconstruction and analysis of the neutrino interactions in the OPERA bricks. The algorithms have been developed, tested and optimized using Monte Carlo simulations. We have used the simulation of the experimental test PEANUT, made at Fermilab, which utilised the NuMI neutrino beam line.

This work is organized as follows.

The first chapter introduces the formalism of neutrino oscillations and discusses the main experimental results on solar, atmospheric and long baseline accelerator neutrinos.

The second chapter decribes, the OPERA experiment, its layout, its performances and the first OPERA test run with the CNGS neutrino beam.

The first part of the third chapter illustrates the basic nuclear emulsion properties and their use in OPERA; the second part describes the European Scanning System, and its performances.

The fourth chapter is dedicated to the description of the algorithms developed for the analysis of OPERA emulsions; their performances are determined using MonteCarlo simulated events.

Chapter 1

Neutrino oscillations

1.1 Introduction

The idea of the neutrino came to life in 1930 by J.W. Pauli as an attempt to explain the continuous spectrum of β decay and solve the problem of non-conservation of momentum and energy in radioactive decays. He proposed that the missing energy in such processes could be carried by a neutral particle that he wished to call "neutron", with spin 1/2 obeying the exclusion principle. This was in a letter to the Tubingen congress [1]. In 1932 Chadwick discovered the neutron and solved the problem of spin and statistics of nuclei but the neutron was too heavy to correspond to the particle imagined by Pauli. In 1933 E. Fermi formulated a theory for calculating the simultaneous emission of an electron with a neutrino, so including Pauli's hypotetical particle. At Solvay conference in Bruxelles in October 1933 Pauli said about this particle: *"... their mass can not be very much more than the electron mass. In order to distinguish them from heavy neutrons, mister Fermi has proposed to name them neutrinos. It is possible that the proper mass of neutrino be zero... It seems to me plausible that neutrinos have a spin 1/2... We know nothing about the interaction of neutrinos with other particles of matter and with photons: the hypothesis that they have a magnetic moment seems to me not funded at all".* In 1933 it was shown that the neutrino mass was very much lower than electron mass; in the same year the discovery of the positron and the beta plus radioactivity confirmed the neutrino idea.

Fermi assumed the neutrino hypothesis to formulate a theory of weak interactions. This theory gave a great deal of credibility to the neutrino hypothesis, but it became necessary to find a concrete proof of the existence of neutrinos. The problem was that neutrinos could penetrate several light years of ordinary matter before interacting. It became clear that large detectors were needed to overcome the neutrino interaction probability. The discovery of neutrinos was due to Reines and Cowan (1955) [2] at Los Alamos. They used an intense flux of anti-neutrinos from a nuclear reactor; the neutrinos interacted in a target made of ∼400 lt of water and cadmium chloride dissolved in it. The detection of antineutrinos was made through the inverse β decay reaction $\overline{\nu_e} + p \rightarrow n + e^+$. The predicted cross section for the reaction was 6×10^{-44} cm^2 and they measured 6.3×10^{-44} cm^2. Their results were published in 1956.

Later, the experiment of Lederman, Schwartz and Steinberger [3] showed the existence of two different kinds of neutrinos, ν_e e ν_μ, associated respectively to the electron and to the muon.

In 1973 neutral currents (neutrino interactions in which a neutrino is not transformed into an electron or a muon) were discovered at CERN and confirmed at Fermilab.

In 1978 in e^+e^- collisions at SLAC was found the evidence for the τ^- lepton to which a third neutrino ν_τ might be associated. The indirect evidence of ν_τ came in the study of the Z boson decay width at the e^+e^- LEP collider which provided a strong indication for the existence of three and only three families of neutrinos [4]. The direct observation of the ν_τ was made only in 2001 at Fermilab in the DONUT experiment [5].

The experimental studies of neutrino properties contributed to formulate the Standard Model (SM) of strong and electroweak interactions of Glashow [6], Weinberg [7] and Salam [8], which describes the experimental results obtained till now. Even so, the community of high energy physicists started looking for physics beyond the SM. The studies of solar and atmospheric neutrinos proved the existence of neutrino oscillations, thus neutrinos must have non zero masses.

1.2 Neutrino mass terms

The Standard Model was formulated in the 60's on the basis of the knowledge of the existing elementary particles and of their interactions. The fundamental particles are organized in three families of quarks

$$\begin{pmatrix} u_L \\ d_L \end{pmatrix}, \quad \begin{pmatrix} c_L \\ s_L \end{pmatrix}, \quad \begin{pmatrix} t_L \\ b_L \end{pmatrix}, \quad u_R, \quad d_R, \quad c_R, \quad s_R, \quad t_R, \quad b_R \tag{1.1}$$

and of leptons

$$\begin{pmatrix} e_L \\ \nu_e \end{pmatrix}, \quad \begin{pmatrix} \mu_L \\ \nu_\mu \end{pmatrix}, \quad \begin{pmatrix} \tau_L \\ \nu_\tau \end{pmatrix}, \quad e_R, \quad \mu_R, \quad \tau_R \tag{1.2}$$

The left-handed fermions transform as doublets under the electroweak SU(2) gauge group; the right-handed particles are singlets. No right-handed neutrinos were included in the SM; only neutrinos which couple to the W and Z bosons were assumed. Consequently, according to the SM there is neither mixing nor CP violation in the lepton sector. But we know now that neutrinos oscillate and therefore that they do have masses. In order to accomodate the neutrino mass with the same Higgs mechanism that generates the masses of quarks and charged leptons, we have to add a ν_R field in the SM, and a Yukawa coupling like $-f_\nu \varphi \overline{\nu_L} \nu_R$ when φ developes its average in vacuum; this coupling carries to the Dirac mass term

$$L_D = -f_\nu \langle \varphi \rangle_0 \overline{\nu_L} \nu_R + h.c. \tag{1.3}$$

that provides a neutrino mass $m_\nu = f_\nu \langle \varphi \rangle_0$. This term conserves the lepton number L that distinguishes neutrinos and negatively charged leptons on one side, from anti-neutrinos and positively charged anti-leptons on the other side. Furthermore, the SM interactions conserve the leptonic number for each family, L_e, L_μ, L_τ. Each neutrino mass eigenstate ν_i differs from its antiparticle in the sense that $L(\overline{\nu_i}) = -L(\nu_i)$. If $\nu_i \neq \overline{\nu_i}$ the neutrino is said to be a *Dirac neutrino*. Since the neutrino is an

electrically neutral particle it is possible to introduce also a Majorana mass term which can be made up of ν_L only and is:

$$L_M^L = -\frac{m_\nu^L}{2}\overline{\nu_L^c}\nu_L + h.c. \tag{1.4}$$

or of ν_R only, in that case we define the Majorana right-handed mass:

$$L_M^R = -\frac{m_\nu^R}{2}\overline{\nu_R^c}\nu_R + h.c. \tag{1.5}$$

ν^c is the charge conjugated of ν. ν_R^c and ν_R are not the mass eigenstates but just the neutrinos in terms of which the model is constructed. The term $m^R\overline{\nu_R^c}\nu_R$ induces $\nu_R \longleftrightarrow \nu_R^c$ mixing. As in the case of $K^0 \longleftrightarrow \overline{K^0}$ mixing, the neutral K mass eigenstates are $K_{S,L} \cong \frac{(K^0+\epsilon\overline{K^0})}{\sqrt{2}}$; so the mixing of $\nu_R \longleftrightarrow \nu_R^c$ yields the neutrino mass eigenstate $\nu_i = \nu_R + \nu_R^c$. An electrically charged fermion cannot have a Majorana mass term because such a term would convert it into an anti-fermion, violating the charge conservation principle. This is not true for the electrically neutral neutrinos; the right-handed field ν_R unlike ν_L carries no electroweak isospin, thus no SM principle prevents the occurrence of a Majorana mass term. Consequently, if the neutrino contains a Dirac neutrino mass term, it can contain also a Majorana neutrino mass term. If the neutrino does not contain a Dirac mass term the Majorana mass term would be the only contribution to the neutrino mass.

1.3 Neutrino masses

The study of neutrino oscillations offers a very sensitive test of neutrino mass differences.The observation of a non vanishing neutrino mass, which follows directly from the observation of neutrino oscillations, is a clear example of new physics beyond the SM. Neutrino oscillation experiments can give information on the square mass differences not on masses. The latter have to be determined in a different way. Up to now neutrino masses have been investigated in two manners:

- direct mass determination using weak decays

- Neutrinoless double beta decay experiments which investigate neutrino masses, but in the case of Majorana neutrinos

In the direct method the neutrino mass is determined using the relativistic energy-momentum relation and $m^2(\nu)$ is the observable in most cases. Actually the neutrino masses are for ν_1, ν_2, ν_3, while ν_e, ν_μ, ν_τ are linear combinations of ν_1, ν_2, ν_3 (see section 1.4). Thus it is not really correct to talk about masses for the flavor eigenstates; but are still quoted these numbers.

Through the investigation of the kinematics of weak decays the electron energy spectrum of a β decay is still the most sensitive model-independent direct method to determine the ν_e mass. The present upper limit for the electron neutrino mass has been determined by investigating the shape of the tritium β spectrum near its endpoint. The result obtained by the Mainz [10] and Troitsk [11] experiments yield to the value

$$m(\overline{\nu}_e) < 2.3\ eV (95\%\ C.L.) \tag{1.6}$$

The KATRIN experiment [12] plans to explore $m(\overline{\nu}_e)$ down to about 0.2-0.3 eV. Measurements of the neutrino mass from the supernova SN1987a fixed a generally accepted upper limit that does not exceed $5.7eV$ [9]. Unfortunately nearby supernova explosions are too rare and not too well understood to allow further improvements.

The upper bound for the ν_μ mass has been determined by measurements of the muon momentum from the decay $\pi^+ \rightarrow \mu^+ \nu_\mu$ at rest [13]. It was found

$$m(\nu_\mu) < 0.17\ MeV (95\%\ C.L.) \tag{1.7}$$

The upper bound for the ν_τ mass comes from measurements done by the LEP experiments [14] of the distribution of the effective mass of five pions in the decay $\tau \rightarrow 5\pi + \nu_\tau$:

$$m(\nu_\tau) < 18.2\ MeV\ \ (95\%\ C.L.) \tag{1.8}$$

1.3.1 Astrophysical limits

The latest high precision CMBR data of the WMAP satellite experiment [15] combined with the large scale structure data of the Galaxy Redshift Survey [16] and other astronomical data [17] allow to place an upper bound on the sum of neutrino masses:

$$\sum_k m_k < 0.71\ eV\ \ (95\%\ C.L.) \tag{1.9}$$

1.3.2 Neutrinoless double beta decay

As mentioned above, another laboratory way to access the neutrino mass scale is the search for the neutrinoless double β decay. This process is essentially the decay of 2 neutrons (protons) into 2 protons (neutrons) within a nucleus at the same time. Usually 2 electrons (positrons) and 2 neutrinos are emitted. In the case that the neutrino is a Majorana particle, the double β decay could occur without emission of any neutrino according to the process $(A, Z) \rightarrow (A, Z+2) + 2e^-$ that violates L_e conservation. It can be shown that the amplitude for neutrinoless double β decay is

$$|\ \langle m_{ee} \rangle\ | = \sum_i |U_{ei}^2 \cdot m(\nu_i)| \tag{1.10}$$

often referred to the $effective\ Majorana\ mass\ for\ 0\nu\beta\beta$ [18].

The Heidelberg-Moscow experiment (1990-2003) [19] used 5 low-background, highly-enriched and high resolution ^{76}Ge detectors (about 11 Kg) in the Gran Sasso underground laboratory; no $0\nu\beta\beta$ signal was observed; they determined the upper limit for $m_\nu < 0.35$ eV (90% C.L.). In December 2001 a subgroup of this collaboration after a recalibration and using more statistics claimed evidence for an experimental signal with $m_\nu = 0.17 - 0.63$ eV (99.73% C.L.)[20] with the best fit value of 0.39 eV. Several neutrinoless double beta decays new generation experiments use different tecnhiques to increase sensitivity and statistics:

- CUORE [21] is an approved cryogenic experiment with 19 towers of 52 detectors, each a 760-g TeO_2 bolometer. This detector would use natural Te,

containing 33.8% ^{130}Te. A pilot experiment CUORICINO [22] corresponding to "one CUORE tower" has given first negative results ($m_\nu < 0.2 - 1.1$ eV)

- The MOON experiment [23] will utilize 1÷3 tons of Mo foils, isotopically enriched to 85% in ^{100}Mo. The ^{100}Mo foil is interleaved with plastic scintillators. It will have coincidence and tracking capabilities to search for $0\nu\beta\beta$ decay as well as solar neutrinos.

1.4 Oscillation phenomenology: in vacuum

Neutrino oscillations were introduced for the first time by Bruno Pontecorvo [24] in 1957 in the case of massive neutrinos and leptonic mixing, but he was thinking about $\nu \leftrightarrow \overline{\nu}$ oscillations. Here we treat the compelling evidences for neutrino oscillations; other exotic possibilities are possible though as subdominant mechanisms, such as neutrino decay, decoherence, or Lorentz invariance violation. Let us extend the SM to include mass and mixing: if neutrinos have masses let us consider three neutrino mass eigenstates ν_1, ν_2, ν_3 and three flavor eigenstates ν_e, ν_μ, ν_τ. If the leptons mix, the weak interaction coupling the W$^\pm$ boson to a charged lepton and a neutrino, is able to couple any flavor eigenstate ν_e, ν_μ, ν_τ. Leptonic W^+ decay can yield a particular charged-antilepton l^+_α ($\alpha = e, \mu, \tau$) associated to a ν_i (i=e, μ, τ). The amplitude for this decay to produce the specific combination $l^+_\alpha + \nu_i$ is $U*_{\alpha i}$, where U is the unitary leptonic mixing matrix.The neutrino of flavor "α" is defined as a superposition of mass eigenstates ν_i:

$$|\nu_\alpha\rangle = \sum_i U^*_{\alpha i} |\nu_i\rangle \tag{1.11}$$

Some models include also a sterile neutrino that is a neutrino, which experiences none of the known forces in nature except gravity (but the experimental results on solar and atmospheric neutrinos as well as KamLAND and K2K disfavour this possibility [25]).

Let us consider the case of vacuum oscillations assuming that the state ν_α is a linear combination of mass eigenstates ν_i. Let us consider how this ν_α evolves in

time by applying the Schroedinger equation to a mass eigenstate

$$|\nu_i(\tau_i)\rangle = e^{-i(m_i\tau_i)}\,|\nu_i(0)\rangle \tag{1.12}$$

where τ_i is the time in the frame of ν_i. In terms of the time t and position L in the laboratory frame the phase factor can be written

$$e^{-im_i\tau_i} = e^{-i(E_it-p_iL)} \tag{1.13}$$

where E_i and p_i are the energy and the momentum of ν_i respectively. Considering the neutrino a relativistic particle it is interesting to evaluate the evolution of this phase phactor for $t \approx L$: $exp[-i(E_i - p_i)L]$. Let us imagine that the neutrino ν_α is produced with a momentum p, so that all the mass eigenstates have the same momentum. The energy E_i of the component ν_i will be $\sqrt{p^2+m_i^2} \approx p + m_i^2/2p$. We have assumed a mass m_i much smaller than the momentum. Then the phase phactor becomes $exp[-i(m_i^2/2p)]$. What happens is that after the neutrino ν_α has travelled a distance L, its vector state is

$$|\nu_\alpha(L)\rangle \approx \sum_i U^*_{\alpha i} e^{-i(m_i^2/2E)L}\,|\nu_i\rangle \tag{1.14}$$

where $E \cong p$ is the average energy of the mass eigenstates. Since the matrix U is unitary we can invert equation (1.11) and insert the result in Eq. (1.14). We find

$$|\nu_\alpha(L)\rangle \approx \sum_\beta \left[\sum_i U^*_{\alpha i} e^{-i(m_i^2/2E)L} U_{\beta i}\right] |\nu_\beta\rangle \tag{1.15}$$

The neutrino born with a single specific flavor ν_α, after a macroscopic distance L in vacuum, turns into a superposition of all flavors. The probability $P(\nu_\alpha \to \nu_\beta)$ that ν_α oscillates into another flavor β is given by $|\langle\nu_\beta|\nu_\alpha(L)\rangle|^2$. Using the unitarity of the mixing matrix U, we find that

$$\begin{aligned} P(\nu_\alpha \to \nu_\beta) = \delta_{\alpha\beta} - 4\sum_{i>j} \Re(U^*_{\alpha i}U_{\beta i}U_{\alpha j}U^*_{\beta j}) \sin^2[1.27\Delta m^2_{ij}(L/E)] + \\ 2\sum_{i>j} \Im(U^*_{\alpha i}U_{\beta i}U_{\alpha j}U^*_{\beta j}) \sin[2.54\Delta m^2_{ij}(L/E)] \end{aligned} \tag{1.16}$$

Here $\Delta m^2_{ij} \equiv m^2_i - m^2_j$ in eV^2, L is in km and E in GeV. Assuming $\hbar = c = 1$ we have

$$\Delta m^2_{ij}(L/4E) \cong 1.27 \Delta m^2_{ij}(eV^2) \frac{L(km)}{E(GeV)} \tag{1.17}$$

If all the neutrino masses, and consequently all the splittings Δm^2_{ij} vanish then $P(\nu_\alpha \to \nu_\beta) = \delta_{\alpha\beta}$. Furthermore from Eq. (1.15), it is clear that in the absence of mixing, the matrix U is diagonal and vanishes if $\beta \neq \alpha$. Thus the oscillation in vacuum implies both masses and mixing. Finally Eq.(1.16) shows the sinusoidal behavior of the probability as a function of L/E. Assuming CPT invariance

$$P(\overline{\nu_\alpha} \to \overline{\nu_\beta}) = P(\nu_\alpha \to \nu_\beta) \tag{1.18}$$

However, from (1.16), we see that

$$P(\nu_\beta \to \nu_\alpha; U) = P(\nu_\alpha \to \nu_\beta; U^*) \tag{1.19}$$

thus,

$$P(\overline{\nu_\alpha} \to \overline{\nu_\beta}; U) = P(\nu_\alpha \to \nu_\beta; U^*) \tag{1.20}$$

That is, the probability for $\overline{\nu_\alpha} \to \overline{\nu_\beta}$ is the same as for $\nu_\alpha \to \nu_\beta$, when U is replaced by U^*. But this means that if U is not real, then $P(\overline{\nu_\alpha} \to \overline{\nu_\beta})$ differs from $P(\nu_\alpha \to \nu_\beta)$ by a reversal of the last term of Eq. (1.15). This difference is a violation of CP invariance; CP invariance would require that $\nu_\alpha \to \nu_\beta$ and $\overline{\nu_\alpha} \to \overline{\nu_\beta}$ have equal probabilities.

The unitary matrix U is usually parametrized in the following manner

$$U = \begin{bmatrix} 1 & 0 & 0 \\ 0 & c_{23} & s_{23} \\ 0 & -s_{23} & c_{23} \end{bmatrix} \begin{bmatrix} c_{13} & 0 & s_{13}e^{-i\delta} \\ 0 & 1 & 0 \\ -s_{13}e^{i\delta} & 0 & c_{13} \end{bmatrix} \begin{bmatrix} c_{12} & s_{12} & 0 \\ -s_{12} & c_{12} & 0 \\ 0 & 0 & 1 \end{bmatrix} \begin{bmatrix} e^{i\alpha_1/2} & 0 & 0 \\ 0 & e^{i\alpha_2/2} & 0 \\ 0 & 0 & 1 \end{bmatrix}$$

$$= \begin{bmatrix} c_{12}c_{13}e^{i\alpha_1/2} & s_{12}c_{13}e^{i\alpha_2/2} & s_{13}e^{-i\delta} \\ (s_{12}c_{23} - c_{12}s_{23}s_{13}e^{i\delta})e^{i\alpha_1/2} & (c_{12}c_{23} - s_{12}s_{23}s_{13}e^{i\delta})e^{i\alpha_2/2} & s_{23}c_{13} \\ (s_{12}s_{23} - c_{12}c_{23}s_{13}e^{i\delta})e^{i\alpha_1/2} & (-c_{12}s_{23} - s_{12}c_{23}s_{13}e^{i\delta})e^{i\alpha_2/2} & c_{23}c_{13} \end{bmatrix} \tag{1.21}$$

Here, $c_{ij} = \cos\theta_{ij}$ and $s_{ij} = \sin\theta_{ij}$, and θ_{12}, θ_{13} and θ_{23} are the three mixing angles. The CP-violating phase δ would lead to $P(\overline{\nu_\alpha} \to \overline{\nu_\beta}) \neq P(\nu_\alpha \to \nu_\beta)$, while α_1 and

α_2 are the CP-violating Majorana phases. These phases have consequences only if neutrinos are Majorana particles. The phase α_i is associated with the neutrino mass eigenstate ν_i in the way that $U_{\alpha i} = U^0_{\alpha i} exp(i\alpha_i/2)$ for all flavors α. So from Eq.(1.15) we can see that the two Majorana phases don't affect neutrino oscillations, regardless of whether neutrinos are Majorana or Dirac particles. Thus if $\nu_i \neq \overline{\nu_i}$, only the phase δ can cause CP violation in neutrino oscillations.

Let us consider now for simplicity the case of neutrino oscillations between two neutrino flavors; in this situation there will be only a single splitting Δm^2, and the mixing matrix can be parametrized as a rotation in terms of one mixing angle θ

$$U = \begin{bmatrix} \cos\theta & \sin\theta \\ -\sin\theta & \cos\theta \end{bmatrix} \tag{1.22}$$

so that the transition probability may be written as

$$P(\nu_\alpha \to \nu_\beta) = \sin^2 2\theta \sin^2\left(\frac{\Delta m^2 L}{4E}\right) \tag{1.23}$$

while the surviving probability of a neutrino of flavor ν_α can be written as

$$P(\nu_\alpha \to \nu_\alpha) = 1 - \sin^2 2\theta \sin^2\left(\frac{\Delta m^2 L}{4E}\right) \tag{1.24}$$

1.5 Neutrino flavor change in matter

The probability that a neutrino of energy E ∼few MeV gets scattered while crossing the earth is about 10^{-12}. Neutrinos can travel through matter without being significantly absorbed, but the presence of matter can affect significantly their propagation. This phenomenon has an analogy in optics: for a transparent medium (air, water) we can neglect its capability of absorbing light but we have to take into account that it can reduce its speed according to the formula $v_{mat} = c/n$ where n is the refractive index of the medium. In some materials or in the presence of an external magnetic field, n is different for different polarizations of light. A similar thing happens for neutrinos: matter is made up of electrons instead of muons or τ; ν_e interacts differently with respect to ν_μ and ν_τ, giving rise to a flavor-dependent refraction index. The neutrino coherent forward scattering from ambient matter interferes with

neutrino propagation: as a result, the probability of changing flavor can be different than in vacuum. This effect in known as Mikheyev-Smirnov-Wolfenstein [26]. It is convenient to treat neutrino propagation in matter via a Schroedinger equation which governs the evolution of a neutrino state vector multi-component, in flavor space. The effective Hamiltonian in the equation, a matrix H in neutrino flavor space, differs from its vacuum counterpart by an addition of an interaction term arising from the coherent forward scattering of neutrinos with ambient electrons. This scattering is mediated by the W boson described by such a potential (for the $\nu_e - \nu_e$ element of H)

$$V = \sqrt{2} G_F N_e \tag{1.25}$$

where G_F is the Fermi constant and N_e the number of electrons per unit volume. In addition, the $\nu_e - \nu_e$, $\nu_\mu - \nu_\mu$, $\nu_\tau - \nu_\tau$ elements of H all contain a common interaction energy coming from the forward scattering mediated by Z exchange. If we do not consider the possibility of transition to a sterile neutrino flavor, this common interaction term adds to H a multiple of identity matrix and this addition does not have any effect on the flavor transitions.

The effect of matter is illustrated by the propagation of solar neutrinos through solar matter. When combined with information on atmospheric neutrino oscillations, the experimental bounds on short-distance oscillation of reactor $\bar{\nu}_e$ tell us that, if there are no sterile neutrinos, then only two neutrino mass eigenstates, ν_1 and ν_2, are significantly involved in the evolution of the solar neutrinos. Correspondingly, only two flavors are involved: the ν_e flavor with which every solar neutrino is born, and the effective flavor ν_x, which is a linear combination of ν_μ and ν_τ.

1.6 Classification of neutrino oscillation experiments

Neutrino oscillation experiments may be classified as:

- **Disappearance**. These experiments, measure the neutrino flux of a certain

flavor l at different distances from the source. In this case, the oscillations in all flavors is studied through the measurement of the surviving probability (eq. 1.24).

- **Appearance**. These experiments, starting from a neutrino beam of a certain flavor search for the presence of a different neutrino flavor in a detector placed at a distance L from the source. In this case the appearance probability is evaluated (eq. 1.23). Up to now, only disappearance experiments have been realized.

An oscillation experiment is characterized by the typical neutrino energy E_ν(GeV) and the source-detector distance L(km). The ratio L/E_ν establishes the Δm^2 range to which an experiment is sensitive:

- **Short baseline (SBL)**: in such experiments the source-detector distance is short, so oscillations can be detected for $\Delta m^2 L/4E \gtrsim 0.1$ leading to a sensitivity of $\Delta m^2 \gtrsim 1\ eV^2$. There are two kinds of SBL experiments: reactor $\overline{\nu_e}$ disappearance experiments with $L \sim 10$ m, $E \sim 1$ MeV, and accelerator ν_μ experiments with $L \lesssim 1$ km, $E \gtrsim 1$ GeV.

- **Long-baseline (LBL)**: in these experiments the source-detector distance is large, giving $\Delta m^2 \gtrsim 10^{-4}\ eV^2$. Atmospheric neutrino experiments (Kamiokande, IMB, Super-Kamiokande, Soudan-2, MACRO) detect neutrinos which travel a distance from about 20 km (downward-going) to about 12780 km (upward-going) and cover a wide energy spectrum, from about 200 MeV to about 100 GeV. K2K and MINOS too are long baseline accelerator experiments.

- **Very long-baseline (VLBL) and solar experiments**: the reactor $\overline{\nu_e}$ disappearance experiment KamLAND with $\overline{L} \sim 180$ km, $E \sim 3$ MeV, yielding $L/E \sim 3 \times 10^5\ eV^{-2}$. KamLAND is sensitive to $\Delta m^2 \gtrsim 3 \times 10^{-5}\ eV^2$.

  The sensitivity of solar neutrino experiments extends over the very wide range $10^{-8}\ eV^{-2} \lesssim \Delta m^2 \lesssim 10^{-4}\ eV^{-2}$.

1.7 Experimental results

In this section we review the main results of neutrino oscillation experiments and their Δm^2 measurements. I shall not discuss the results of several SBL oscillations experiments, which probed scales of $\Delta m^2 > 1\ eV^2$. In order to analyze the data on neutrino oscillations we need a framework with three neutrinos; this because there is a strongly favoured mass hierarchy of the splittings $|\Delta m^2_{12}| \ll |\Delta m^2_{23}|$. Furthermore the mixing angle θ_{13} which couples the two oscillations is small. We can divide the current knowledge on neutrino mixing parameters into:

- oscillations with Δm^2_{12} and θ_{12} from solar neutrino experiments;
- oscillations with Δm^2_{23} and θ_{23} from atmospheric and long baseline accelerator neutrino experiments;
- limits on θ_{13}.

1.7.1 Solar neutrinos

The central part of the Sun, like all the stars, behaves as a fusion reactor, transforming protons into He^4 nuclei through the global process

$$4p \rightarrow He^4 + 2e^- + 2\nu_e \tag{1.26}$$

with an energy release per fusion $E(pp) \approx 27$ MeV. The total neutrino flux Φ_ν at the Earth can be obtained from the total thermal power of the Sun which is directly related to the measurable solar constant $S = 8.5 \times 10^{11}\ cm^{-2}s^{-1}$ at the Earth and $\phi_\nu = 6.5 \times 10^{10}\ cm^{-2}s^{-1}$. The emitted neutrino spectrum depends on the details of the energy producing solar cycle. Precise knowledge of the spectrum is important in the interpretation of the experimental solar neutrino data.

The spectrum from the Standard Solar Model (SSM) [27] is shown in Fig. 1.1. Two kinds of solar neutrino experiments have been performed: radiochemical and electronic on real-time. Radiochemical experiments are based on the reaction

$$(A, Z) + \nu_e \rightarrow (A, Z + 1) + e^- \tag{1.27}$$

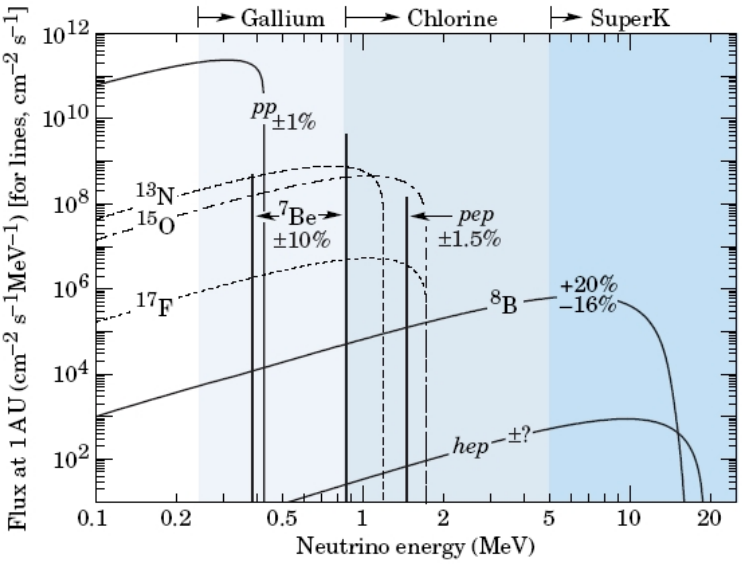

Fig. 1.1: The solar neutrino spectrum predicted by the standard solar model.

where the daughter nucleus is unstable and decays with a "reasonable" half-life. The production rate of the daughter nucleus is given by

$$R = N \int \Phi(E)\sigma(E)dE \tag{1.28}$$

where Φ is the neutrino flux from the Sun, N is the number of atoms in the target and σ the cross section for the reaction (1.27).

- **Homestake**

  The first solar neutrino experiment was the chlorine experiment of Davis *et al.* [28], placed in a gold mine in South Dakota (USA). It started in 1968 and ran till 1996. The reaction used to detect neutrinos is

  $$\nu_e + {}^{37}Cl \rightarrow {}^{37}Ar + e^- \tag{1.29}$$

  which has an energy threshold of 0.814 MeV. With this threshold the experiment is not able to measure pp neutrinos. The target, made up of a tank of 615 t perchloro-ethylene (Cl_2Cl_4), was exposed to solar neutrinos at a depth

of 4100 m.w.e. The natural abundance of ^{37}Cl is about 24% so that the number of the target atoms is 2.2×10^{30}. The produced argon atoms are volatile in the solution and are extracted about every 60-70 days and collected in a cooled charcoal trap. The trapped Ar atoms are then purified, and inserted into small proportional counters. These are placed in a very low activity lead shielding in order to observe the Ar decays. The result, after more than 20 years measuring time, was $2.56 \pm 0.16 \pm 0.15 \quad SNU$. [1] This is about 1/3 the value predicted by the SSM:

$$\frac{\Phi_{Cl}^{Hom}}{\Phi_{Cl}^{SSM}} = 0.34 \pm 0.03 \tag{1.30}$$

- **Kamiokande** and **Super-Kamiokande**

  The Kamiokande experiment [29] consisted by a cilindric tank, whose internal surface was covered with photomultipliers; it was filled with 4.5 kt of pure water; it was situated in the Kamioka mine (Japan) at a depth of 2700 m.w.e. Since 1995 it was replaced with Super-Kamiokande (SK) [30] similar to it, but with ten times larger volume and a higher density of photomultipliers. Solar neutrinos are detected in real-time through the elasting scattering process:

$$\nu_e + e^- \rightarrow \nu_e + e^- \tag{1.31}$$

  The electron identification is carried out by detecting the Cherenkov light ring in the water. The effective threshold for this reaction is 7 MeV in Kamiokande and 6.5 MeV in SK. The Cherenkov light detection is in real-time; therefore it is possible to study also possible variations of the neutrino flux due to seasonal variations or night/day effects. Because of the high thresholds, Kamiokande and SK measured only the small flux of ^8B neutrinos. They obtained respectively the results:

$$\Phi(^8B) = 2.80 \pm 0.19 \pm 0.33 \times 10^6 \quad cm^{-2}s^{-1} \qquad \text{Kamiokande (final)} \tag{1.32}$$

$$\Phi(^8B) = 2.35 \pm 0.02 \pm 0.08 \times 10^6 \quad cm^{-2}s^{-1} \qquad \text{Super-Kamiokande} \tag{1.33}$$

[1] 1 Solar Neutrino Unit = 10^{-36} captures per target atom per second

The SK flux, obtained in 2002, is 46.5% of the SSM prediction, i.e.

$$\frac{\Phi^{SK}}{\Phi^{SSM}} = 0.465 \pm 0.015 \tag{1.34}$$

- GALLEX/GNO [31] and SAGE [32] are sensitive to pp neutrinos (see fig. 1.1). The detection occurs through the reaction

$$\nu_e + {}^{71}Ga \rightarrow {}^{71}Ge + e^- \tag{1.35}$$

These radiochemical experiments collected few atoms of ^{71}Ge in a target of tens of tons of $GaCl_3$ in Gallex/GNO and metallic Ga in SAGE. They detected the decays of^{71}Ge in small proportional counters. The threshold for the reaction was 0.233 MeV; therefore GALLEX and SAGE were sensitive to almost all the solar neutrino flux coming from the process $2p \rightarrow d + e^+ + \nu_e$. GALLEX was running in the underground Gran Sasso lab from 1991 to 1997; after some maintenance and upgrades it was renewed as GNO. SAGE performed data taking between 1990 and 2001 in the Baksan underground laboratory. Both experiments confirmed the deficit of solar neutrinos

$$74.1^{+5.4+4.0}_{-5.4-4.2} \quad SNU \qquad \text{GALLEX/GNO} \tag{1.36}$$

$$70.8^{+5.3+3.7}_{-5.2-3.2} \quad SNU \qquad \text{SAGE} \tag{1.37}$$

with respect to the ν capture rate in ^{71}Ga predicted by the SSM 128^{+9}_{-7} SNU.

- **SNO**

The Sudbury Neutrino Observatory [33] was built in Canada and started running in 1999. It was a real-time Cerenkov detector using about 1000 t of heavy water (D_2O) at a depth of 2000 m in the Creighton mine at Sudbury (Ontario). The (D_2O) was placed in a transparent acrylic tank and surrounded by 9700 photomultipliers mounted on a geodesic support structure surrounding the heavy water tank. The threshold of SNO was about 5 MeV. Neutrinos coming from ^8B decay were detected through the processes:

$$\nu_{\mathrm{e}} + d \rightarrow p + p + \mathrm{e}^- \qquad \text{(CC)} \qquad \mathrm{E_{min}} = 1.44\,\mathrm{MeV}$$

$$\nu_{\rm s} + d \rightarrow p + n + \nu_{\rm s} \qquad (NC) \qquad E_{min} = 2.23\ MeV$$
$$\nu_{\rm s} + {\rm e}^- \rightarrow \nu_{\rm s} + {\rm e}^- \qquad ({\rm ES})$$

The first reaction is a charged weak current process (CC) and is sensitive only to ν_e, while the second one (neutral current, NC) and the third one (elastic scattering, ES) involve all the three neutrino flavors. The third process is less sensitive to ν_μ and ν_τ. In the second reaction, neutrons are detected via the 6.3 MeV gamma-rays produced in the reaction

$$n + d \rightarrow^3 H + \gamma \tag{1.38}$$

In order to improve the detection efficiency of neutrons, and consequently the NC flux measurement, some Cl (2 t of NaCl) was added to the heavy water to use the gamma-rays up to 8.6 MeV from the neutron capture reactions.

The first measurement by SNO of the CC process gave

$$\Phi_{CC}(^8B) = 1.75 \pm 0.07(stat) \pm 0.12(sys) \pm 0.05(theor) \times 10^6 cm^{-2} s^{-1} \tag{1.39}$$

which is significantly smaller than the value measured by Super-Kamiokande. This is an indication that other active neutrino flavors come from the Sun and participate into the scattering processes. The total neutrino flux measured by the neutral current process is

$$\Phi_{NC} = 5.09^{+0.44}_{-0.43}(stat.)^{+0.46}_{-0.43}(sys.) \times 10^6 cm^{-2} s^{-1} \tag{1.40}$$

and is in a good agreement with the SSM as well as the result obtained using the data set with salt to enhance NC sensitivity

$$\Phi_{NC}^{Salt} = 5.21 \pm 0.27(stat.) \pm 0.38(sys.) \times 10^6 cm^{-2} s^{-1} \tag{1.41}$$

The measurement obtained with the ES processes is consistent with that of Super-Kamiokande.

- **KamLAND**

  The Kamioka Liquid-scintillator Anti-Neutrino Detector [34], located in the Kamioka mine, confirmed the SNO results using anti-neutrinos from nuclear

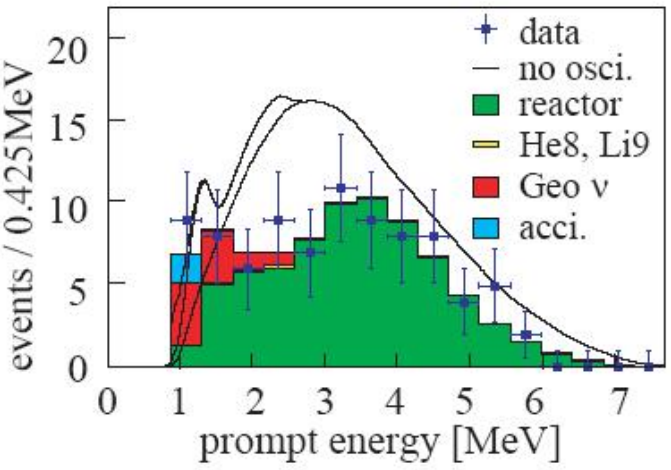

Fig. 1.2: KamLAND experiment. Positron energy spectrum from $\overline{\nu_e}$ candidate events with associated background spectra. The dashed vertical line indicates the analysis cut used to remove the geological antineutrinos

reactors placed in Japan and in South-Korea at an average distance of 180 km from the detector. It is a sort of long-baseline experiment with a large L/E ratio, which can give a good sensitivity in the $\Delta m^2 \sim 10^{-5}\ eV^2$. The detector used 1 kton of pure liquid scintillator, surrounded by about 2000 photomultipliers, in order to measure the reaction

$$\nu_e + p \rightarrow e^+ + n \tag{1.42}$$

The prompt signal comes from the Cherenkov light produced by the e^+, with a threshold at 1.8 MeV. The 2.22 MeV gamma-ray from neutron capture on hydrogen is delayed. Prompt-delayed events correlation in space and time give a clean signature that reduces accidental background.

The energy spectrum of the data collected by KamLAND is given in Fig. 1.2 compared with the expectations in absence of oscillations. While the expected number of neutrino events above 2.6 MeV is 86.8 ± 5.6 they observed only 54 events. The ratio

$$\frac{N_{obs} - N_{bg}}{N_{expected}} = 0.611 \pm 0.085\ (stat) \pm 0.041\ (sys),$$

indicates a deficit of neutrino events consistent with $\overline{\nu_e}$ oscillations.

The combined solution for the oscillation parameters from solar neutrino experiments and KamLAND provided a best fit value

$$\Delta m^2_{12} = 7.9^{+0.5}_{-0.5} \times 10^{-5} \quad eV^2 \tag{1.43}$$

$$\tan^2(2\theta_{12}) = 0.40^{+0.10}_{-0.07} \tag{1.44}$$

1.7.2 Atmospheric neutrinos

In the interactions of cosmic rays (protons and nuclei) with the atmosphere many pions and kaons are produced and they decay into neutrinos

$$C.R. + Air \rightarrow \pi^{\pm}/k^{\pm} + X$$

$$\pi^{\pm}/k^{\pm} \rightarrow \mu^{\pm} + \nu_{\mu}(\overline{\nu_{\mu}})$$

$$\mu^{\pm} \rightarrow e^{\pm} + \nu_e(\overline{\nu_e}) + \nu_{\mu}(\overline{\nu_{\mu}})$$

In first approximation, there are 2 ν_{μ} per ν_e. The atmospheric neutrino flux predictions suffer from large uncertainties ($20\% - 30\%$), due to the uncertainty of the absolute value of the cosmic ray flux and to the uncertainty of the cross sections for cosmic ray interactions with nuclei in the atmosphere. This difficulty was partially overcome in the early experiments by measuring the ratio of ratios

$$R \equiv \frac{[N(\nu_{\mu} + \overline{\mu_{\mu}})/N(\nu_e + \overline{\nu_e})]_{data}}{[N(\nu_{\mu} + \overline{\mu_{\mu}})/N(\nu_e + \overline{\nu_e})]_{theo}} \tag{1.45}$$

where "data" and "theo" are respectively the measured and Monte Carlo calculated ratios. In absence of oscillations $R \equiv 1$. The experiments that measured the ν_{μ} and ν_e interactions in terms of the double ratio R were

- *Nusex* [35], *Frejus* [36] and *Soudan* [37], that used tracking calorimeters
- *IMB* [38], *Kamiokande* [39] and *SuperKamiokande* [40] that used water Cherenkov detectors.

Experiment	R
NUSEX	$0.99^{+0.35}_{-0.25}$
Fre′jus	$1.00 \pm 0.15 \pm 0.08$
IMB	$0.54 \pm 0.05 \pm 0.11$
Kamiokande(sub-GeV)	$0.60^{+0.06}_{-0.05} \pm 0.05$
Kamiokande(multi-GeV)	$0.57^{+0.08}_{-0.07} \pm 0.07$
Super-Kamiokande(sub-GeV)	$0.658 \pm 0.016 \pm 0.032$
Super-Kamiokande(multi-GeV)	$0.702 \pm 0.031 \pm 0.099$

Tab. 1.1: Double ratio results from atmospheric neutrino experiments

The results are shown in table 1.1. As we see, except Nusex and Frejus, whose results were in agreement with expectations, the double ratios measured by the other experiments were smaller than expectations. Later SoudanII and SuperK confirmed the anomaly in the ν_μ/ν_e double ratio for contained events.

SoudanII [41] used a fine grained tracking and shower calorimeter of 1 kton, situated at a depth of 2100 m.w.e. in the Soudan mine. The main results were obtained from the analysis of the fully contained events coming mostly from quasi-elastic neutrino reactions. After background correction the double ratio obtained for the whole zenith angle range ($-1 \leq \cos\theta \leq +1$) is $R = 0.69 \pm 0.12$ consistent with the hypothesis of oscillations.

MACRO

The MACRO experiment [42] using a different technique reported a measurement of upthroughgoing muons coming from interactions in the rock below the detector of neutrinos of $\overline{E}_\nu \sim 50$ GeV. The analysis showed an anomalous zenith angle distribution and a deficit of the total number of upgoing muons. The ν_μ detected via charged current interactions ($\nu_\mu \rightarrow \mu$) were identified by means of streamer tubes (for tracking) and scintillator planes (to measure the time of flight of particles). The L/E_ν distribution has shown a distortion with respect to MC simulation without oscillations. The observed effect are highly in favour of the $\nu_\mu \rightarrow \nu_\tau$ oscillation scenario, while the $\nu_\mu \rightarrow \nu_{sterile}$ hypothesis was rejected at 99.8% C.L. MACRO obtained a global best fit result with $\Delta m^2_{23} = 2.3 \times 10^{-3}\ eV^2$ for maximal mixing,

$\sin^2 2\theta_{23} = 1$. Fig. 1.3 shows the zenith angle distribution of the upthroughgoing muons compared with different MC oscillation calculations. From the figure (a) it is evident that the new MC predictions for the oscillated flux, using the recent fit of the primary cosmic ray energy distribution yield a neutrino flux which is too low in comparison to the measured upwardgoingmuons [2]. Fig. (b) and (c) refer to topologies induced by low energy neutrinos ($E_\nu \simeq 2 - 3$ GeV). The comparison of the data with the predictions confirms the oscillations with the same parameters of the upthroughgoing sample.

The zenith angle of an upthroughgoing muon, provides a measure of the neutrino path-length L; a measurement of the muon energy was made by means of Multiple Coulomb Scattering of induced muons in the MACRO rock absorbers. This allows to estimate the L/E_ν ratio. The ratio data/MC (in the no oscillation hypothesis) as a function of the estimated L/E_ν for the upward-going-muon sample is shown in fig. 1.4. Also this analysis is in favour of $\nu_\mu \rightarrow \nu_\tau$ oscillations.

In the last papers, in order to reduce the effect of the MC problems, MACRO used the following three ratios which were verified to be MC independent, for the events:

- Upthroughgoing muons: zenith distribution ratio: $R_1 = N_{vert}/N_{hor}$
- Upthroughgoing muons: E_ν estimate by Coulomb MS: $R_2 = N_{low}/N_{high}$
- Low energy events: $R_3 = (Data/MC)_{IU}/(Data/MC)_{ID+UGS}$.

By fitting the three ratios to the $\nu_\mu \rightarrow \nu_\tau$ oscillation formulae, MACRO obtained the best fit values of $\Delta m^2_{23} = 2.3 \times 10^{-3}\ eV^2$ and $\sin 2\theta_{23} = 1$. Using the Bartol96 flux, it is possible to add the informations on the absolute flux values of the upthroughgoing

[2]The simulation of atmospheric neutrino events requires physics generators based on atmospheric neutrino fluxes and neutrino cross sections. The absolute normalization is still uncertain and this uncertainty increases with energy. In the past, unidimensional Monte Carlo codes were used, at present, three dimensional Monte Carlo predictions for neutrino fluxes and a new fit of the primary cosmic ray flux, are available. All these Monte Carlos provide the same shape of the angular distributions for the ν_μ flux. The absolute value predicted by the new Monte Carlo is ∼25% too low at high energies and ∼12% at low energies with respect to experimental data. This difference is probably due to the use of a new fit of the primary cosmic ray data

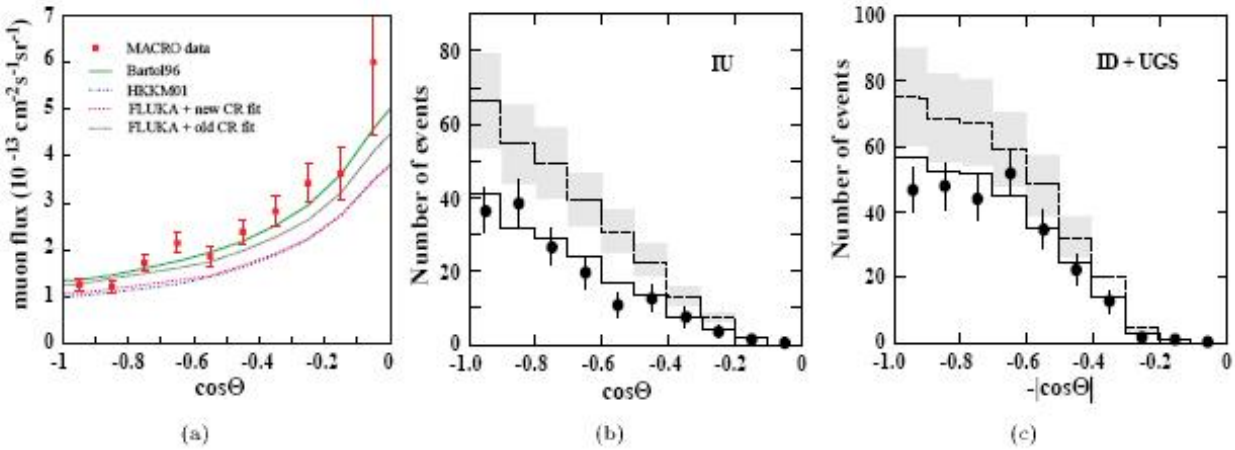

Fig. 1.3: MACRO: (a) Comparison between the measured angular distribution of the *UpThroughGoing* muon flux and the MC oscillated predictions given by Bartol96 (solid curve), HKKM01 (dash-dotted line), FLUKA fitted to to new CR measurements (dashed-curve) and FLUKA with the old CR fit (dotted curve). Zenith distributions for (b) IU ans for (c) ID+UGS events (black points) compared with the no oscillation Bartol96 MC (dashed line with a scale error band) and with the ν_μ-oscillation predictions, with maximal mixing and $\Delta m^2 = 0.0023$ eV^2.

data and of the low energy semicontained muon data. Also these ratios favour $\nu_\mu \to \nu_\tau$ oscillations.

SuperKamiokande

Atmospheric neutrinos are detected in the SuperKamiokande (SK) experiment by measuring the Cherenkov light released by the charged particles produced in the neutrino CC scattering on nucleons (free protons and oxygen nuclei). A relativistic charged lepton travelling in water generates a detectable Cherenkov ring. By measuring the Cherenkov light SK reconstructs the energy E_l and the direction θ_l of the scattered charged lepton. The scattered proton is not visible because its energy is below the water Cerenkov threshold. The large mass of the detector and the possibility of defining a large inner volume allows SK to collect high statistics. They classified their events as *fully contained* events up to ~ 5 GeV; these events can be further subdivided into: sub-GeV and multi-GeV events with energies below and

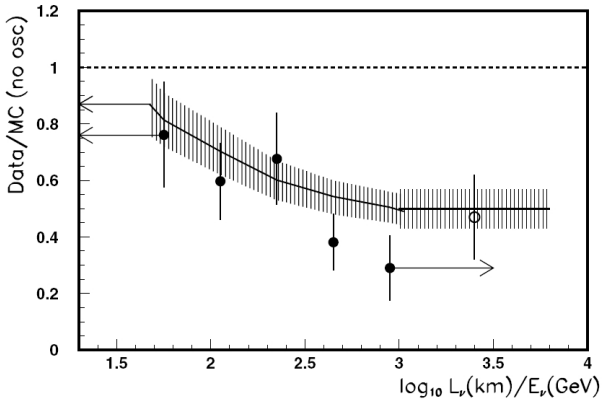

Fig. 1.4: MACRO: ratio data/MC$_{(no oscillations)}$ as a function of the estimated L/E$_\nu$ for the *UpThroughGoing* muon sample (black points). The solid line is the MC expectation assuming $\Delta m^2_{23} = 0.0023$ eV^2 and $\sin^2 2\theta = 1$. The last point (empty circle) is obtained from the *InUp* sample.

above 1.33 GeV. The sub-sample defined as partially coantained events is characterized by a filled circle of light. In this case the resolution is worse than for FC events. The last group of events detectable by SK are the so-called upwardgoing muons further divided into stopping muons ($\langle E_\nu \rangle \sim 7$ GeV) and upthroughgoing muons ($\langle E_\nu \rangle \sim$ 70-80 GeV). Note that this average energy is considerably larger than in MACRO. SK took data from 1996 to 2001 (1489 days, terminated by an accident) and since 2004 collected some more events. The results of the analysis are shown in Fig. 1.5. The data and the MC behaviour shows a situation similar to that discussed for MACRO. In particular the electron-like event data (see fig. 1.5(a)) are in agreement with the HKKM95 MC predictions in absence of oscillations, while they are higher than the HKKM01 non oscillated MC. For the muon-like events, the new MC predictions are relatively low, expecially for the high energy upthroughgoing muons. SK obtained the final oscillation parameters making a global fit, where they leave the absolute normalizations as free parameters.

The SK collaboration also studied the muon neutrino disappearance probability as a function of L/E_ν and may have observed a dip in the L/E_ν distribution at $L/E_\nu \simeq 500$ km/GeV. Alternative models that could explain the zenith angle and energy dependent deficit of the atmospheric muon neutrinos are disfavored. The

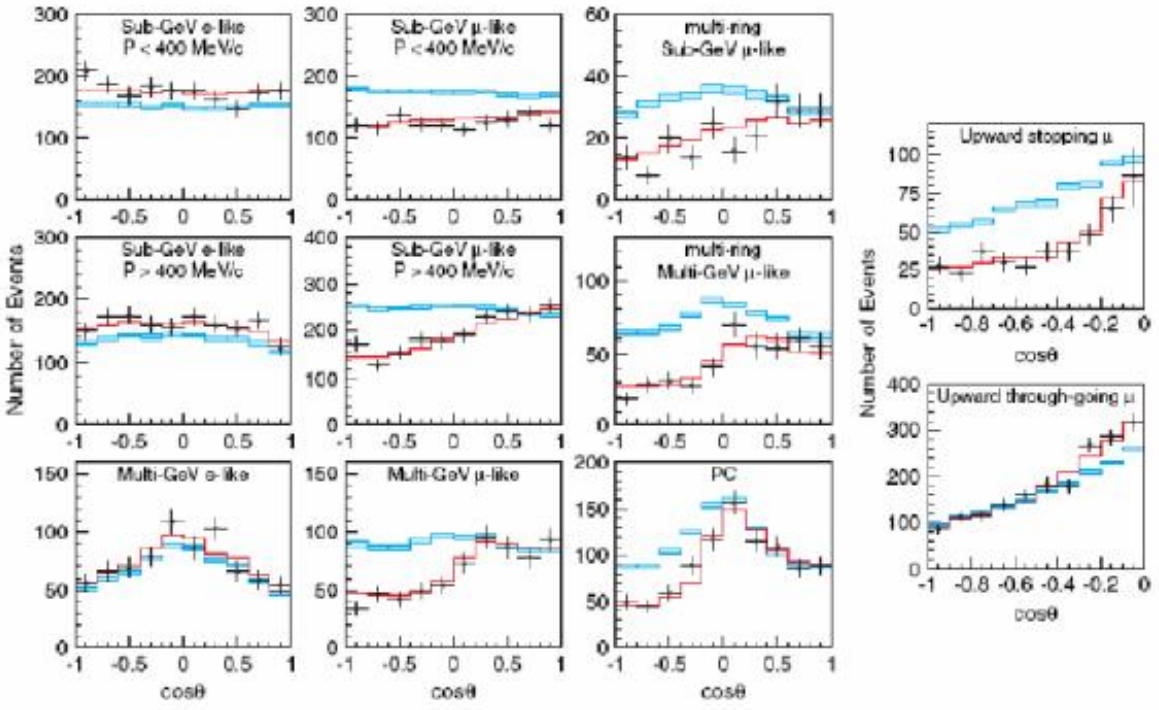

Fig. 1.5: SK data taken since 1996 till 2001 with the detector in full configuration (1489 days for FC+PC events and 1646 days for upgoing μ). Zenith distributions for e-like and μ-like sub-GeV and multi-GeV events, for partially contained events, for upthroughgoing muons and for stopping muons (black points). The boxes are the no oscillation HKKM01 predictions, the lines refer to $\nu_\mu \to \nu_\tau$ oscillations with $\sin^2 2\theta_{23} = 1$ and $\Delta m^2_{23} = 2.4 \times 10^{-3}$ eV^2.

global SK analysis yielded for $\nu_\mu \leftrightarrow \nu_\tau$ oscillations: $1.9 \times 10^{-3} < \Delta m^2_{23} < 3.0 \times 10^{-3}$ eV^2 and $\sin 2\theta_{23} > 0.90$ at 90% C.L.

MACRO and SK searched also for subdominant oscillations violating Lorentz invariance: these were not observed and only limits could be established [43]. Limits on possible decays of solar neutrinos were established in [popa].

1.7.3 Experiments with reactors

The deficit of ν_μs in the atmospheric neutrinos is expected to be due to $\nu_\mu \rightarrow \nu_\tau$ oscillations. The CHOOZ [44] and Palo Verde [45] experiments, detected reactor $\overline{\nu}_e$ through the inverse β decay reaction

$$\overline{\nu}_e + D \rightarrow p + n \tag{1.46}$$

They constrained the $\overline{\nu}_e \rightarrow \overline{\nu}_\mu$ oscillations with the parameter: $\sin^2 2\theta_{13} \leq 0.10$.

1.8 Accelerator long baseline experiments

The hypothesis of neutrino oscillations is strongly supported by solar, atmospheric, reactor and also accelerator long baseline neutrino data.

- **K2K**

  The experiment (KEK to Kamioka) in Japan, used a 12 GeV proton beam from the KEK accelerator to generate a ν_μ beam directed to the SK detector, located 250 km away [46]. The neutrino beam had an average energy of 1.3 GeV. Another detector placed immediately in the neighbourhood of the source gave the possibility of a precise measurement of the ν_μ flux produced. The latest K2K results presented in 2006 and shown in fig. 1.6 are in a good agreement with the expectations based on atmospheric neutrino data; the best fit values are $\sin^2 2\theta = 1.0$ and $1.8 \times 10^{-3} eV^2 < \Delta m^2_{23} < 3.6 \times 10^{-3}$ eV^2.

- **NuMi**

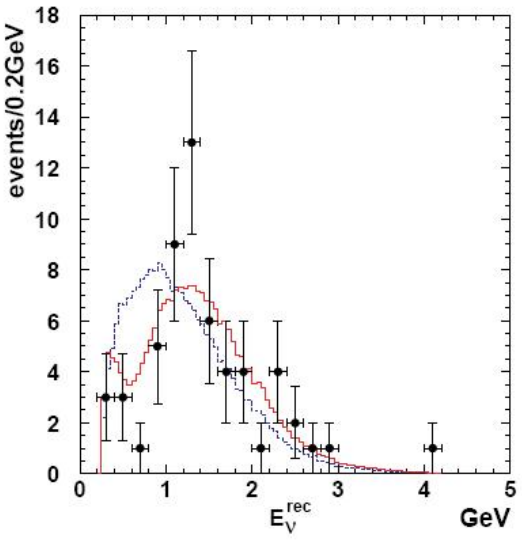

Fig. 1.6: K2K experiment. The reconstructed E_ν distribution for the 1-ring μ-like sample. Points with error bars are data. The solid line is the best fit spectrum with neutrino oscillation ($\Delta m^2_{23} = 2.7 \times 10^{-3}\ eV^2$ and $\sin^2 2\theta_{23} = 1$) and the dashed line is the expectation without oscillation.

The running NuMi-MINOS (Main Injector Neutrino Oscillation Search) uses an intense beam of ν_μ created at Fermilab and directed to the Soudan mine in the Northern Minnesota at a distance of 735 km where a Far Detector is placed at a depth of 714 m [47]. A Near Detector, similar in design to the Far detector, is located 1 km downstream of the target. Both of them can measure the composition and energy spectrum of the beam, allowing precision measurements of the spectral distortion. The Minos Far detector is a 5.4 kton steel scintillator sampling calorimeter made of 2 supermodules separated by a gap of 1.1 m. The Near detector has a total mass of 1 kton. The structure consists of sandwiches of octagonal planes of 2.54 cm thick steel and 1 cm thick plastic scintillators. Each scintillator plane consists of 192 scintillator strips 4 cm wide, and up to 8 m long depending on the position in the plane. The strips in adjacent planes are oriented orthogonally, thereby providing the event reconstruction in two orthogonal coordinates. The scintillation light is collected using wavelength shifting (WLS) fibers embedded within the scintil-

lator strips. The WLS fibers are coupled to clear optical fibers at both ends of a strip and are read out using 16-pixel multianode photomultiplier tubes. Both detectors are equipped with magnet coils which generate ~ 1.2 T toroidal magnetic fields, which act to contain long muon tracks and provide curvature information for estimating energies.

The classes of events considered in MINOS are:

- charged-current ν_μ events consisting of long muon tracks accompanied by short hadronic showers near the event vertex
- neutral-current ν_μ events: short, sparse hadronic showers
- ν_e charged-current events: short, dense electromagnetic showers

Only charged-current ν_μ events were considered in the first analysis; the bulk of the data was taken in the low energy configuration of the beam in order to maximize the sensitivity to the oscillation minimum. The preliminary results from the observed and reconstructed neutrino spectrum at the Far detector show an incompatibility with unoscillated predictions, as shown in fig. 1.7. The signal appears to be consistent with the oscillations seen in the atmospheric and K2K data.

In Tab. 1.2 are reported the best fit values for Δm^2_{23} and $\sin^2 2\theta$ obtained by the atmospheric neutrinos and long baseline experiments.

	$\Delta m^2_{23}(\times 10^{-3})$ eV^2	$\sin^2 2\theta$
SoudanII	5.2	1
MACRO	2.3	1
SK	2.4	1
K2K	2.7	1
MINOS	2.74	1

Tab. 1.2: Summary of the best fit results from the atmospheric and long baseline neutrino experiments.

These experiments have clearly shown the disappearance of muon meutrinos; but there is not yet any evidence of what they become. Only detecting the

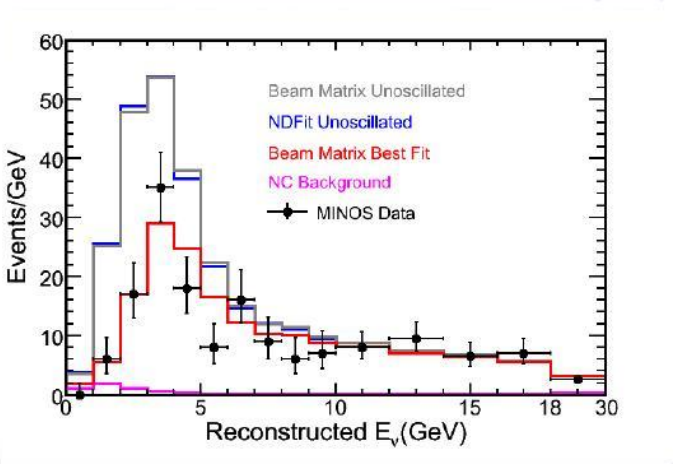

Fig. 1.7: MINOS first results from the Far detector spectrum: the gray histogram shows the predicted spectrum without oscillations, the points are data, the blue histogram represents a fit to the data for no oscillation and the red histogram represents the oscillation hypothesis with the best fit values $\Delta m^2_{23}= 2.74\times10^{-3}$ and $\sin^2 2\theta=1$

appearance of tau neutrinos from a muon neutrino beam will really confirm the current theory of neutrino oscillations as explanation of the atmospheric neutrino anomaly. For this aim the OPERA appearance experiment has been proposed.

Chapter 2

The OPERA experiment

2.1 Introduction

OPERA (**O**scillation **P**roject with **E**mulsion-t**R**acking **A**pparatus), is a proposed long-baseline experiment, in order to observe the ν_τ appearance in a nearly pure ν_μ beam produced at CERN (CNGS, Cern Neutrino beam to Gran Sasso) [48]. The apparatus is located at the Gran Sasso Underground Laboratory, at a distance of 732 km from the beam source. The main purpose is the direct observation of $\nu_\mu \leftrightarrow \nu_\tau$ oscillations in the parameter region indicated by the deficit of atmospheric muon neutrinos and by the zenith angle dependence observed by MACRO, SuperKamiokande and SoudanII experiments

The beam energy has been tuned above the τ lepton production threshold, and has an average value of about 17 GeV. The ν_μ beam is optimized in order to obtain the maximum number of ν_τ charged-current interactions in the detector. In case of a positive signal, the observation of even a few ν_τ will be significant because of the very low expected background. OPERA is searching for ν_τ by detecting the decay of the τ lepton that is produced in the charged-current interactions of the ν_τ with nucleons of the target. It is necessary to have a massive target and a high resolution tracking device with a micrometric resolution to reconstruct the τ decay. The OPERA experiment is a hybrid detector which uses electronic trackers and ECC (see section 2.3.1)In August 2006 the first test run with the CNGS neutrinos

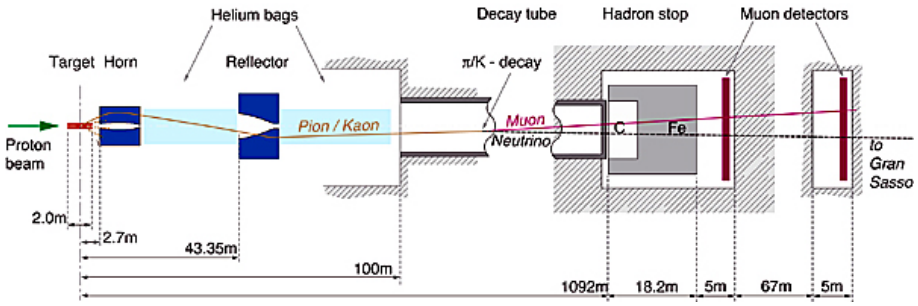

Fig. 2.1: Layout of CNGS neutrino beam

was conducted successfully with a high performance of the electronic detectors of the apparatus.

2.2 The CNGS neutrino beam

The CNGS beam of muon-neutrinos follows the classic scheme of a conventional beam (see Fig. 2.1). An intense proton beam at 400 GeV is extracted from CERN Super Proton Synchrotron (SPS) in 10.5 μs short pulses with intensity of 2.4×10^{13} p.o.t. per pulse [50]. The proton beam is sent towards a target consisting of a series of small graphite cylinders (4 mm diameter) for an overall target length of 2 m. The cylinders absorb the large heat and the thermo-mechanical shock due to the energy deposited by the proton beam. Then the target is cooled with a jet of high pressure helium gas in a closed circuit. The particles produced in the target (pions and kaons with energies between 20-50 GeV) enter a system of magnetic horns which focus positive particles with a mean energy of 35 GeV and defocus negative particles. The aim is to make the beam of pions and kaons as parallel as possible. The first *horn* causes an excessive deflection of charged particles with energies less than 35 GeV and it is insufficient to deflect those particles with energies over 35 GeV. So a second horn called *reflector* placed 40 meters behind, performs the necessary corrections of this effect. The combined focusing effect of the two horns ensures a maximum number of pions and kaons. Helium tubes are placed in the free space before and after the reflector in order to reduce the interaction probability for

secondary hadrons. Pions and kaons are then directed toward a decay tunnel where their decay produces muon neutrinos and muons. In order to avoid any loss of pions and kaons through interactions with air an evacuated tunnel is used. The tunnel contains a steel pipe with a diameter of 2.45 m and 1 km long. The typical decay lengths of pions with energies of 40 GeV/c are about 2.2 km. Located at the end of the tunnel a massive iron hadron stop absorbs all the protons which did not interact in the target together with all pions and kaons that did not decay before reaching this point. Some muons are absorbed in the beam stopper, others are absorbed in the rock behind the hadron stop. The trajectory of the muons produced with the neutrinos is measured in two detection stations: the first is located immediately behind the hadron stop and the second is located after 67 m of rock. The intensity of the SPS proton beam is important to reach the physics goals of the OPERA experiment. In a mode of operation where the SPS is shared wih LHC, 4.5×10^{19} pot can be delivered in 1 year with 200 days run. Fig. 2.2 shows the expected neutrino energy distribution at Gran Sasso, located at 732 km from CERN. The ν_μ flux at Gran Sasso is $3.5 \times 10^{11} + \nu/m^2/year$ with a contamination of about 4% of anti-ν_μ, 0.8% ν_e and less than 0.05% anti-ν_e. The number of CC interactions expected from ν_μ is about 2600/kton/year.

During the whole time duration of the experiment (5 years) about 31000 CC plus neutral current (NC) events will be collected by OPERA from interactions with the lead-emulsion target. Out of them 95 (214) CC ν_τ interactions are expected for $\Delta m^2_{23} = 2 \times 10^{-3} eV^2$ ($3 \times 10^{-3} eV^2$) and $\sin 2\theta_{23} = 1$ [51]. Taking into account the overall ν_τ detection efficiency the experiment should gather 10÷15 signal events with a background of less than one event.

The possibility of increasing the neutrino beam intensity at a moderate cost is under studies by the CNGS design group [52]: it is expected that the maximum intensity in the SPS will be 7×10^{13} rather than 4.5×10^{13} pot/cycle. Further improvements could increase the proton flux by as much as factor 1.5.

The low ν_e ($\overline{\nu_e}$) contamination allows to search for the sub-dominant $\nu_\mu \leftrightarrow \nu_e$ oscillation seeking an excess of ν_e CC interactions.

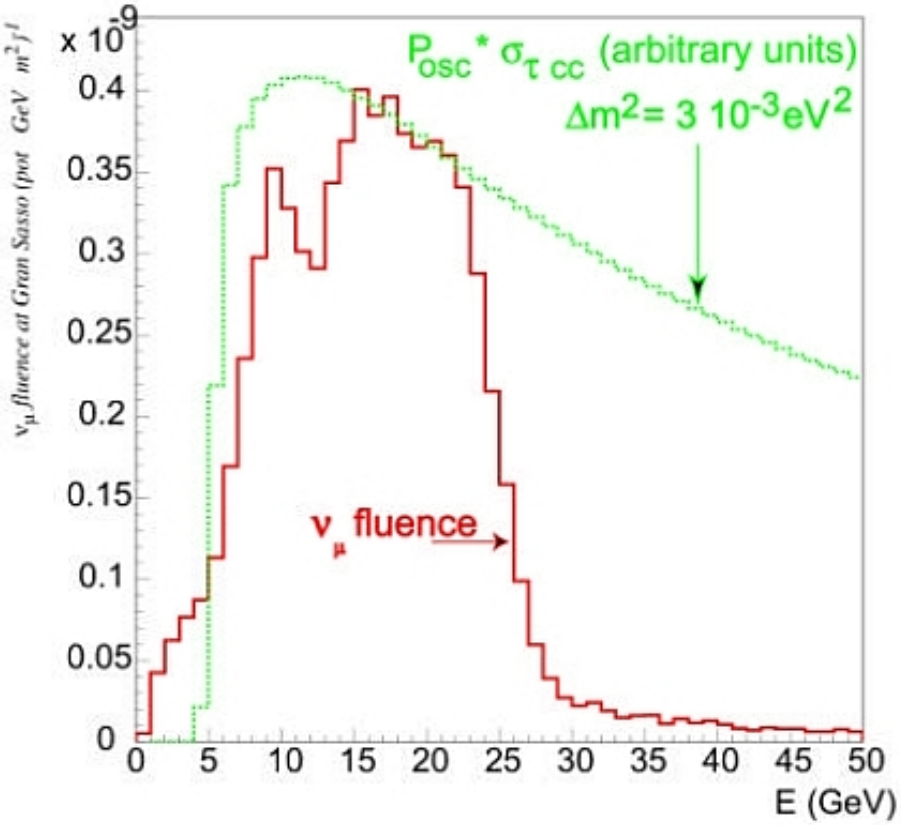

Fig. 2.2: Histogram with dark line: CNGS ν_μ fluence as function of neutrino energy at Gran Sasso. Histogram with thin line: energy dependance of the number of τs produced via CC interactions for $\Delta m^2_{23} = 3.0 \times 10^{-3} eV^2$ and maximal mixing.

2.3 The OPERA detector

OPERA is a massive hybrid detector consisting of 2 identical parts called *super-modules* (SM). Each SM has a target section, made of electronic detectors (target trackers, TT), a lead/emulsion targets, and a muon spectrometer. In front of the first SM is placed a Veto system made of glass Resistive Plate Chambers. Table 2.1 shows the main characteristics of each SM.

Dimensions (m^3)	$\sim$ 6.71(H) x 6.75(W) x 3.75(L) m^3
Thickness of one layer of ECC (mm)	1.3
Number of emulsions films/brick	57 + 1 CS
Brick x-section (cm^2)	10.2 x 12.7
Brick thickness (cm)	7.5 (packing not included)
Brick thickness (X_0)	10
Brick weight (kg)	7.9 (lead) + 0.4 (films) = 8.3
Module thickness (cm)	12
Number of modules/superm.	31
Number of bricks/superm.	103168
Emulsions films surface/superm. (m^2)	$\sim$75000
Superm. weight (ton)	815 (lead) + 41 (films) = 856

Tab. 2.1: Design features of the target section of a supermodule.

The construction of the experiment started in 2003. The first equipped magnet was completed in 2004 together with the first half of the target support structure. The second magnet was completed at the beginning of 2005. In spring 2006 all electronic detectors were installed. Fig. 2.3 shows the general layout of the OPERA detector, while the picture in Fig. 2.4 shows the OPERA status in August 2006 during the first run with CNGS.

2.3.1 Target structure

The basic element of the Pb/emulsion target is the so-called Emulsion Cloud Chamber (ECC): an emulsion sheet consisting of two emulsion layers ($\approx$44 μm thick each) put on either side of a plastic base (205 μm thick) is inserted between lead plates 1 mm thick (see Fig. 2.5). The lead provides the large target mass ($\sim$1.6 ktons)

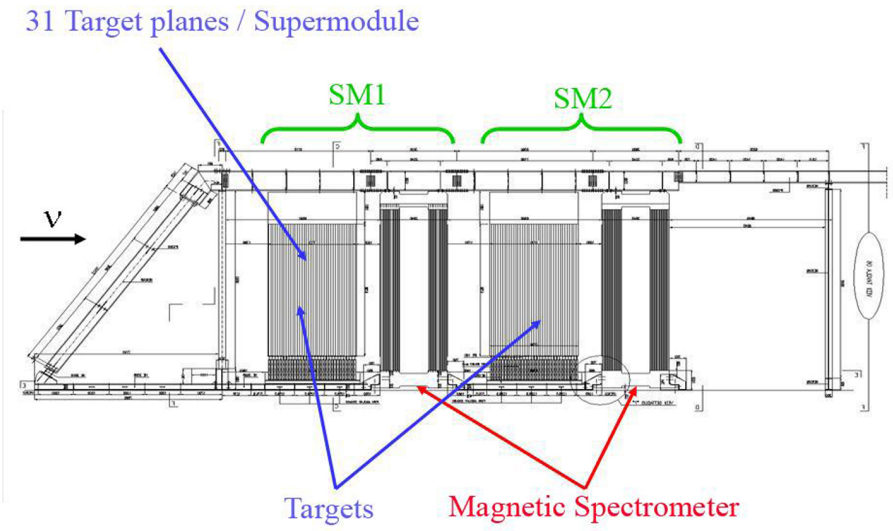

Fig. 2.3: Schematic drawing of the OPERA detector in Gran Sasso

for neutrino interactions. The lead/emulsions are arranged in "bricks": each one is a stack of 56 lead plates interleaved by 57 nuclear emulsion films. The transverse dimension of an ECC brick is 10.2 cm × 12.7 cm while the thickness is 7.5 cm equivalent to 10 X_0 radiation lengths enough to allow electron identification through their electromagnetic showers and momentum measurements by multiple scattering. The weight of a brick is about 8.3 kg. A the downstream end of a brick is attached a doublet of emulsions called *Changeble Sheets* (CS), which can be detached from the rest of the brick for the analysis. The CS doublet is used to better locate the tracks generated by neutrino interactions. The bricks are being produced by a series of automatic robots called BAM (Brick Assembly Machine).

2.3.2 Electronic Target Trackers

The target section is made up of 31 brick walls for each supermodule; each wall is interleaved with 2 electronic Target Tracker planes. Bricks can be removed or inserted in the walls by two automatic robots called Brick Manipulator System (BMS) placed on the lateral sides of the detector. The target section for each SM will contain ∼100000 bricks equivalent to about 900 tons. The main goal of

Fig. 2.4: Picture of OPERA in the Hall C of Gran Sasso

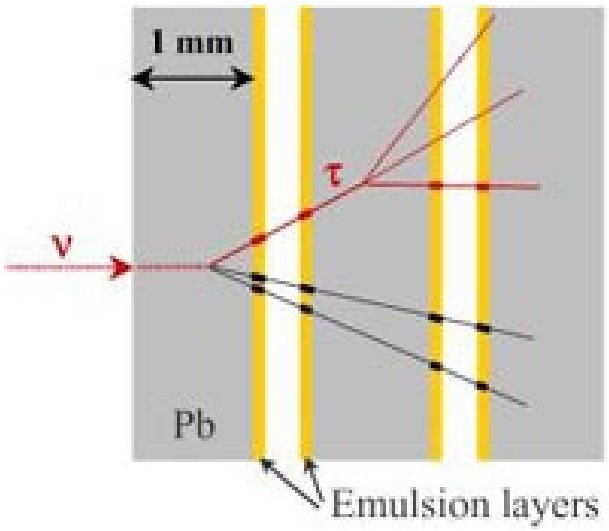

Fig. 2.5: Schematic structure of an ECC cell.

the electronic target planes is to provide a localization of the brick where a neutrino interaction occurred in order to define the region of the emulsion films to be scanned. The CS doublet is used to confirm the brick choice. One TT consists of 2 planes, each made of 4 horizontal and 4 vertical modules that guarantee the x-y coordinate measurement. Each module contains 256 plastic scintillator strips, 6.6 m long, 2.6 cm wide and 1 cm thick, read out at both sides through optical fibers by 64 multi-anode photomultipliers The transverse pointing accuracy is about 1.5 cm for CC events and 3 cm for NC events.

2.3.3 The muon spectrometers

The muon spectrometers perform muon identification and momentum measurements of the muons. Each spectrometer is made up of 2 magnetised iron walls for a total weight of about 1 kton. The magnetic field in the walls is essentially uniform with a measured intensity of 1.52 T. The transverse dimensions of a magnet are 8.75 m horizontally, 10 m vertically and 2.64 m in length. A spectrometer has a good acceptance also for muons originating further upstream.

The magnets are equipped with active detectors: the iron layers are interleaved

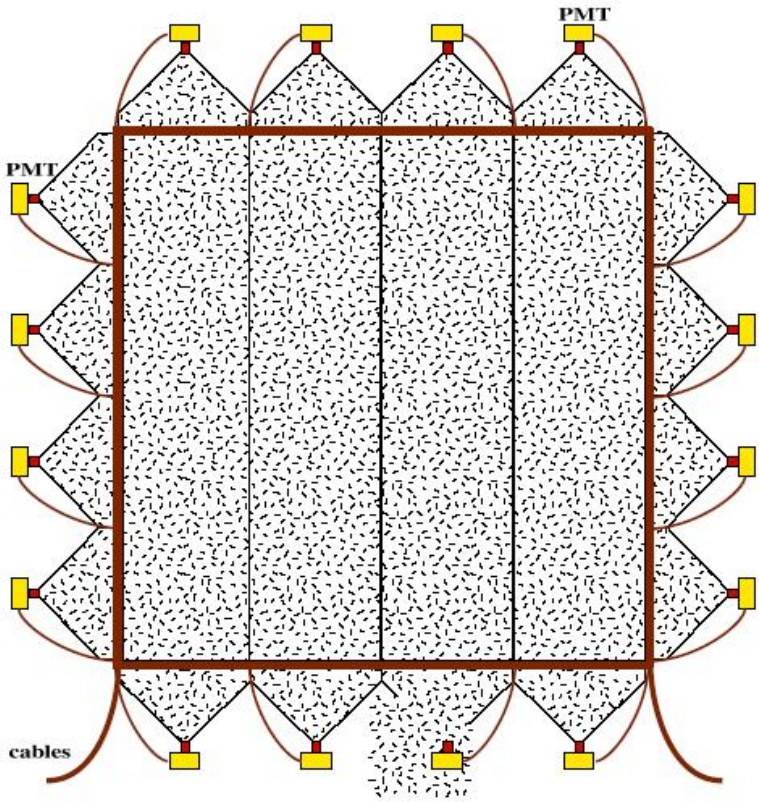

Fig. 2.6: Schematic view of a Target Tracker scintilator plane

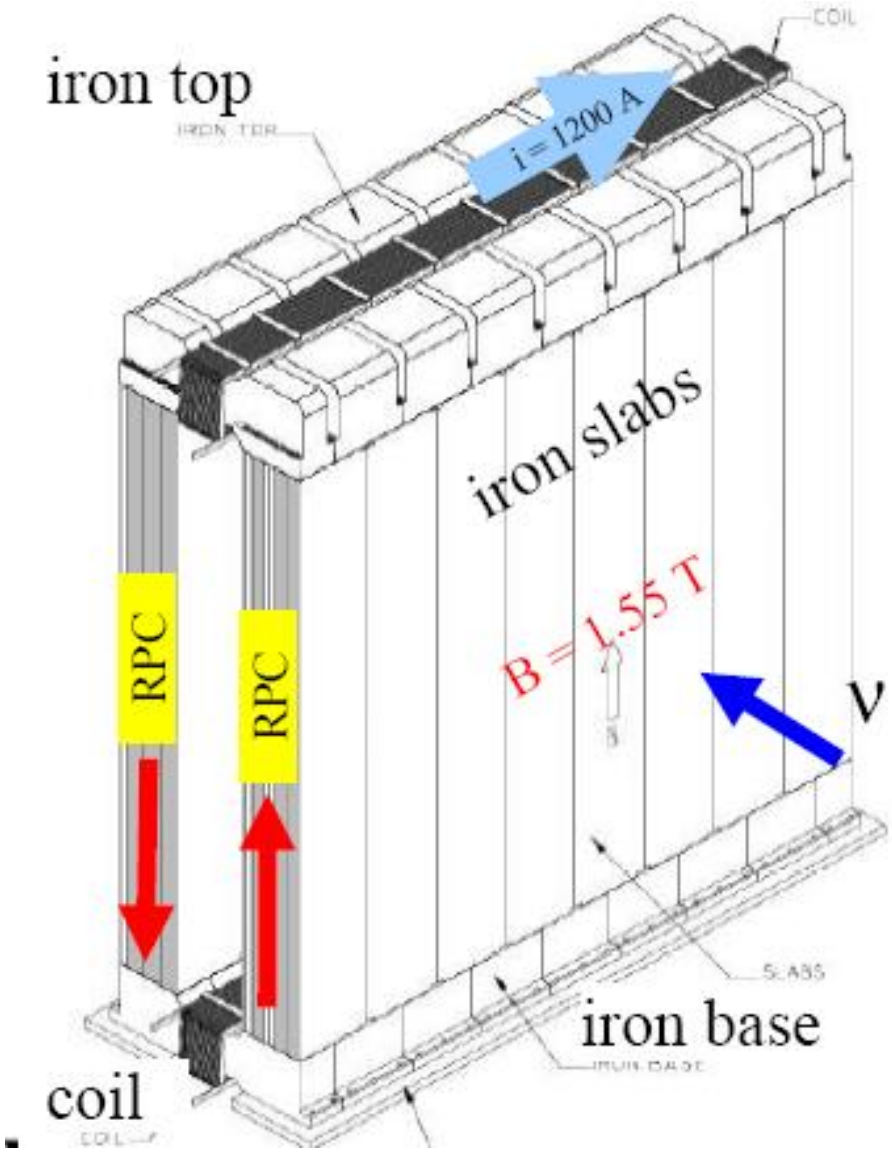

Fig. 2.7: Schenatic view of one dipolar magnet

with RPC planes (Inner Trackers); drift tubes (Precision Trackers, PT) are placed in front, behind and inside the magnet to perform more precise muon momentum measurements and determine with higher accuracy their charge sign. RPC planes, chosen for their high intrinsic geometrical efficiency and low cost identify penetrating muons and measure their charge and momentum in an independent way w.r.t. the drift tubes. Each RPC plane consist of a chamber 2mm thick with two electrode plates made of 2 mm thick bakelite with a high resistivity, painted on the external surfaces with graphite. The induced pulses are collected on two pickup planes made of copper strips 3.5 cm wide and 2.6 cm long, glued to plastic foils located on either side of the chamber. Strips run in two perpendicular directions to provide bi-dimensional coordinate informations. The total number of RPC planes is 11 + 11 inserted between the iron plates of the two arms of each magnet. The Inner Trackers allow a coarse tracking inside the volume of the magnet and facilitate track matching between the PT. They also provide a range measurement of the stopping particles and a calorimetric analysis of hadrons.

The Precision Trackers (PT) consist of vertical drift tube planes made of thin aluminium cylinders with 38 mm outer diameter and 8 m length. Each tube has a central wire of 45 μm diameter. The intrinsic resolution of the tubes is 0.3 mm; due to possible misalignments, we assume an overall resolution on each measured coordinate of 0.5 mm. Each spectrometer is equipped with six 4-fold layers of tubesTo resolve the ambiguity in the track spatial reconstruction each of the two drift tube planes upstream of the magnet is complemented by an RPC plane with pickup strips oriented at about $\pm 45^{\circ}$ called XPC.

The RPC and the TT planes were commissioned in 2006.

2.4 Procedure for runs with the CNGS beam

The synchronization between the detector and the CNGS beam spill is done offline by GPS signal. The detector remains sensitive during the spill intervals and runs in a no-trigger mode. Events detected out of the spills as cosmic-ray muons, environment radioactivity background are used for the monitoring and for the analysis. The

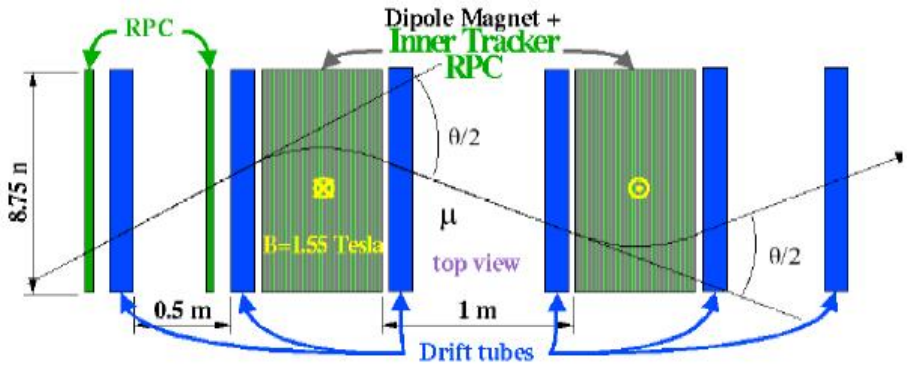

Fig. 2.8: Drift tube planes placed before, inside and behind the spectrometer

cosmic ray muons may yield information on the μ^+/μ^- ratio underground. When running with the CNGS beam, the triggered events are classified (CC-like or NC-like event) by a combined response of Target Tracker and spectrometer detectors. Charged particles from a neutrino interaction in a brick cross the CS and produce a trigger in the TT planes. This trigger localizes the position of the candidate brick; the CS doublet attached to the downstream face of the brick is removed and analyzed without removing the brick. If the CS analysis confirms the neutrino interaction, the brick is removed from the wall and exposed in the external lab to cosmic rays in a pit shielded by 40 cm of iron to minimize the electron component. The aim is to collect penetrating muon tracks for emulsions alignment before the developing procedure [53]. After development the emulsions are sent to the automatic scanning stations for researching the neutrino vertex and the decay kink in the tracks close to the vertex.

2.5 The first OPERA run with CNGS

In August 2006, the first OPERA test run with CNGS neutrinos took place. The beam intensity was lower than the nominal one, with a total integrated flux of 7.6 $\times 10^{17}$ pot for a period equivalent to about 5 days. The CERN accelerators and the OPERA detector were synchronized with GPS signals before starting data-taking with an accuracy better of 100 ns. The run was successfully conducted with

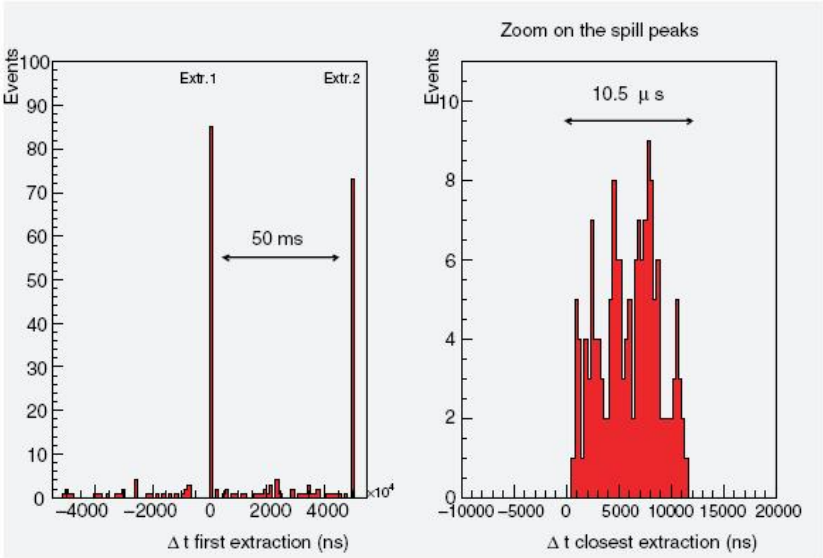

Fig. 2.9: Time distribution of events collected in the two extractions of the same beam pulse during the first OPERA run. The right histogram shows the time distribution of the second extraction.

electronic detectors only, collecting neutrino interactions in the rock upstream of the detector, in the passive material of the mechanical structure and in the iron of the spectrometers. In addition, the information from the tracking plane doublet of emulsion sheets (CS) was used to study the connection between track segments in the emulsion with tracks reconstructed in the TT. During this run the Veto system was not yet operational.

The OPERA detector started data taking from the very first spills of the beam and 319 neutrino events were collected, which are consistent with the 300 events expected for the given integrated intensity mentioned before. The analysis was performed in two ways: the first based on the event timing information and the second based on the reconstruction of track-like events without taking into account the timing information. The event time information represents a basic selection since the time window of the spill is well defined in an interval of 10.5 μs, while cosmic ray background in this time window, corresponds to 10^{-4} of the collected statistics as showed in Fig. 2.9.

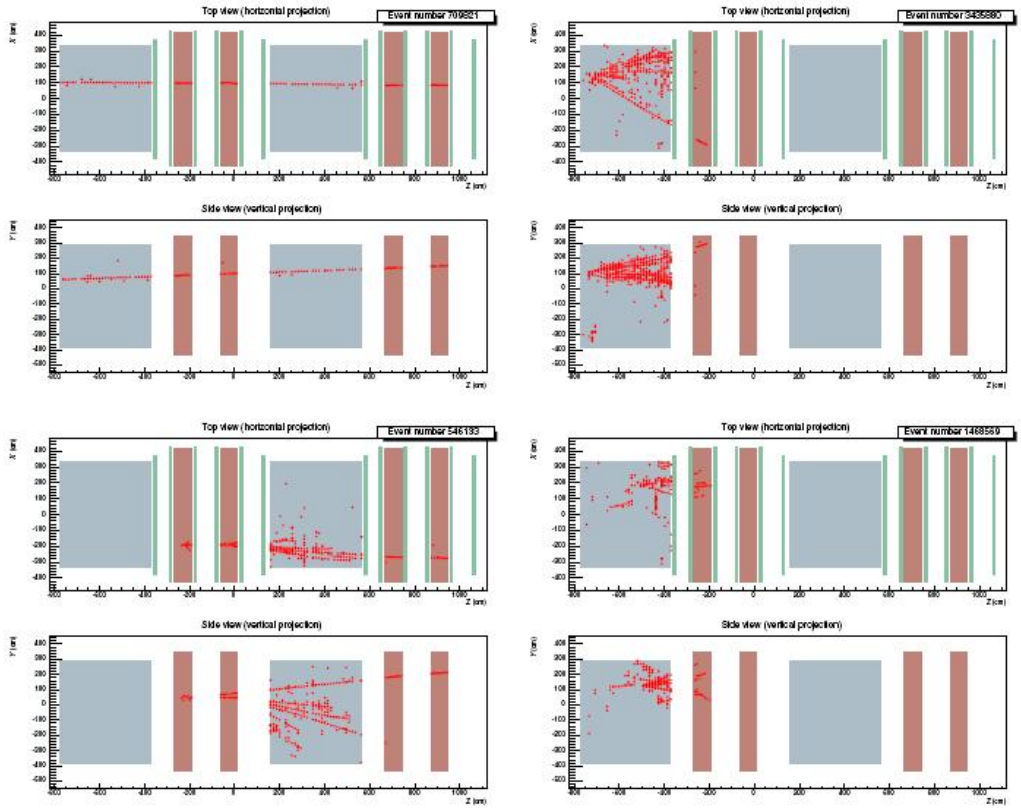

Fig. 2.10: Event display of neutrino interactions from CNGS run. For each events the top and the side view are showed respectively. The SM targets are indicated in blue, the spectrometers in light brown, TT and RPC hits in red.

The second analysis classified neutrino events in the following way:

- CC neutrino interactions in the rock upstream of the detector or in the material present in the hall leading to a penetrating muon track (top-left of Fig 2.10)
- CC and NC neutrino interactions in the target material (top-right and bottom right in Fig. 2.10)
- interactions in the iron of the spectrometers (bottom-left of fig. 2.10)

The angular distribution of the beam-induced and cosmic muon events shown in Fig. 2.11 were obtained by selecting single track events with a minimum number of

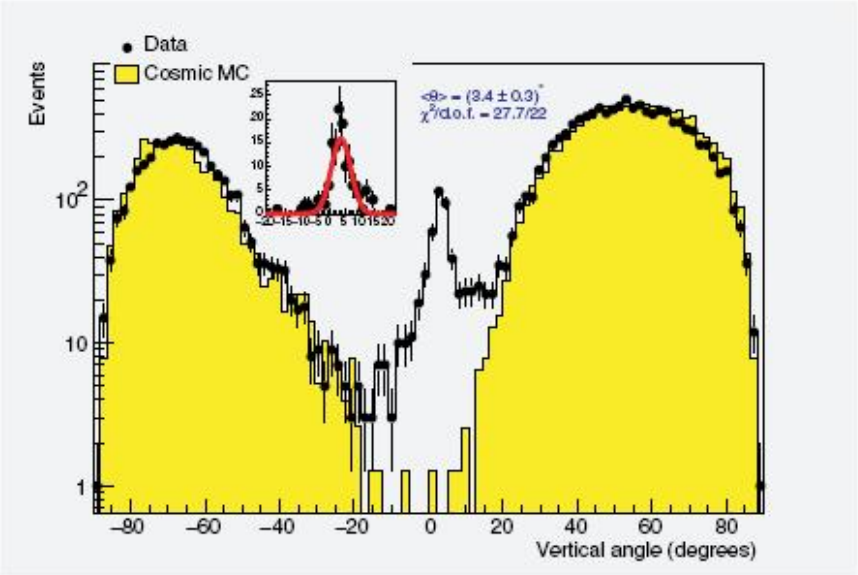

Fig. 2.11: Angular distribution of beam-induced events and of cosmic ray muons taken during the OPERA run with electronic detectors (black dots). The histogram indicates the predictions obtained from MC simulations of cosmic rays. The inset in the picture shows the angular distribution of the beam events.

six layers of fired RPCs in each spectrometer. The histogram of Fig. 2.11 represents the simulated cosmic ray muons. A gaussian fit on the angle of the beam events taken, gives (as shown in the inset of Fig. 2.11) a mean value of (3.4±0.3)° consistent with the expectation of 3.3° for a neutrino beam originating from CERN and travelling underground to the LNGS hall.

Also a test of the connection between muon tracks triggered by TT and those measured in the CS doublet has been successfully performed, in particular the capability of going from the centimeter resolution of the electronics to the micrometric precision of the emulsions was tested. The angular difference in track connection between the TT and CS was better than 10 mrad. An example of track reconstruction is shown in Fig. 2.12.

The success of this first OPERA run with good performances of the electronic detectors is the first step towards the running of the completed detector.

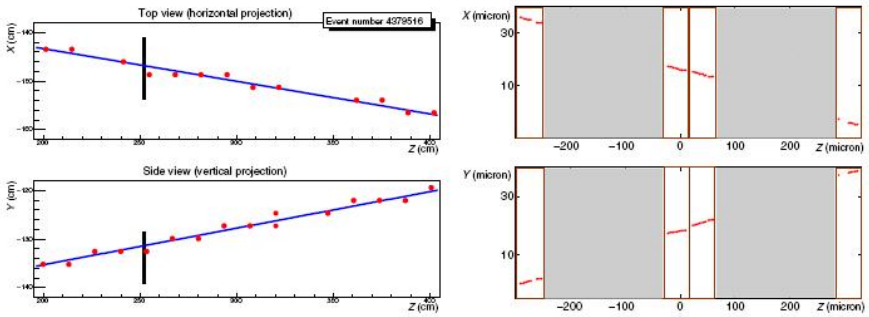

Fig. 2.12: On the left: display of both projections of one event with the muon passing through the CS detector plane. The vertical dark segments indicate the position of the CS doublet crossed by the track. The black dots represent the hits of the electronic detectors closest to the CS plane. On the right: display of the corresponding microtracks reconstructed in the CS doublet.

2.6 Physics performances

The signal of the occurrence of $\nu_\mu \leftrightarrow \nu_\tau$ oscillations is the CC interaction of τ neutrinos in the detector target through the reaction $\nu_\tau N \rightarrow \tau^- X$ which is identified by the detection of the τ lepton in the final state through the decay topology of its modes: $\tau^\pm \rightarrow h, \mu^\pm$ or $e^\pm$. Since the expected event rate is small, it is crucial to separate efficiently the ν_τ CC events from all the other neutrino flavors and to keep the background at a very low level. To this purpose, the detector will allow to identify the event by exploiting the τ decay specific properties, characterized by a short lifetime ($c\tau \approx 87$ μm) and the presence of missing transverse momentum due to the ν_τ in the final state.

The signal detection efficiency of OPERA was estimated on the basis of tests and Monte Carlo simulations. The τ decay modes investigated by OPERA are, the electron, muon and single charged hadron channels:

$$\begin{aligned} \tau^- &\rightarrow e^- \nu_\tau \overline{\nu}_e \\ \tau^- &\rightarrow \mu^- \nu_\tau \overline{\nu}_\mu \\ \tau^- &\rightarrow h^- \nu_\tau (n\pi^0) \end{aligned}$$

The branching ratio (BR) measurements of these three single prong decay modes give

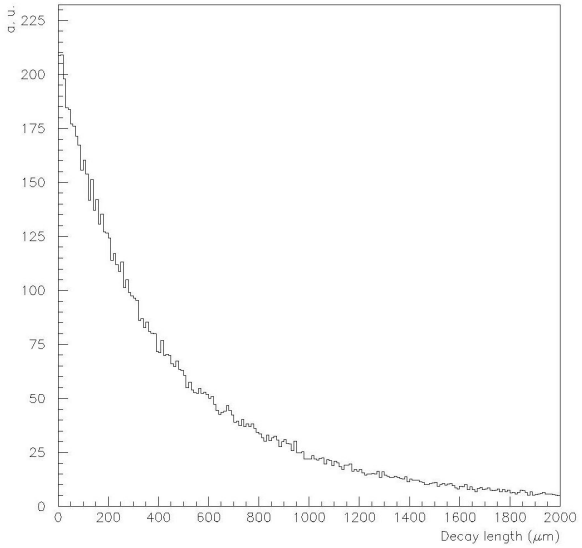

Fig. 2.13: MC τ decay length distribution, obtained assuming the CNGS energy spectrum and the oscillation parameters indicated by the atmospheric neutrinos.

17.8%, 17.7% and 49.5% for the electronic, muonic and hadronic channels. For the typical τ energies expected with the CNGS we obtain the decay length distribution shown in Fig. 2.13.

The τ decays inside the ECCs are classified in two categories: *short and long decays*. In the first case the τ is produced in a lead plate and decays in the same plate. In the second case the decay occurs in the first or second downstream lead plate. For short decays the τ candidates are detected by the measurements of a significant impact parameter (IP) of the daughter track with respect to the tracks originating from the the primary vertex (IP $>$ 5-20 μm). For long decays the τ is detected by measuring the *kink* angle between the charged decay daughter and the parent direction (with $\theta_{kink} \gtrsim$20mrad). The distribution of the τ decay kink angles for the electron channel is showed in fig. 2.14. The τ decay detection into electron channel is strongly favoured by the dense brick structure with a compact cell design; this allows electron identification through its showering in the downstream cells. The main background contribution for this channel is given by charm production

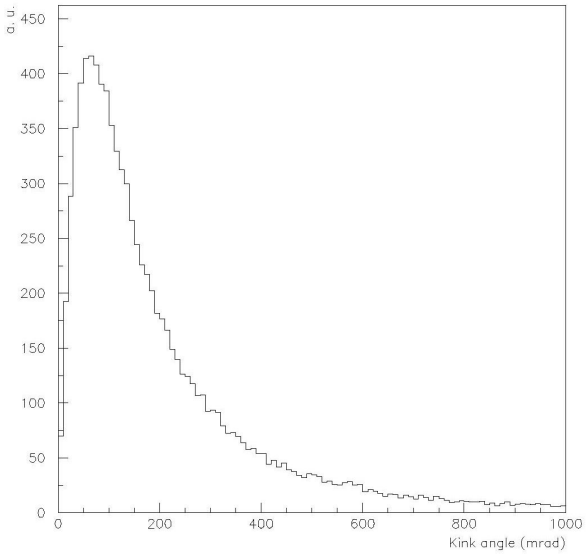

Fig. 2.14: τ kink angle distribution for the $\tau \rightarrow e$ decay mode.

in ν_μ CC interactions. Charmed particles are produced in the CC and NC neutrino interaction processes:

$$\nu_\mu N \rightarrow c\,\mu X \tag{2.1}$$

$$\nu_\mu N \rightarrow c\bar{c}\,\mu X \tag{2.2}$$

$$\nu_\mu N \rightarrow c\bar{c}\,\nu_\mu X \tag{2.3}$$

Charged mesons have masses and lifetimes similar to that of the τ lepton. The processes indicated above constitute a background source to the oscillation signal if the primary muon is not detected in the first reaction, or if the charm partner is not identified in the third or in the second reaction. The most relevant source is represented by single charm production given by the first reaction. In addition to charm production we can include another background source: kink-like events from scattering of primary electrons.

In the muonic channel the presence of penetrating muon tracks allows an easy localization of the event vertex. The potential background from large scattering of muons produced in the ν_μ CC interactions can be reduced to a good level of tolerance by applying topological cuts on the kink angle and on the transverse momentum of

the muon at the decay vertex.

Hadronic decay modes are characterized by the largest BR, but at the same time are affected by a high background due to hadronic reinteractions. It may happen in fact that one of the primary hadrons can interact in the first lead plate simulating the charged single prong τ decay if the other products of the interactions are not detected in the emulsion. In this case it is necessary to reduce this background with strong kinematical cuts. For a beam intensity of $4.5{\times}10^{19}$ $pot/year$, running for 5 years, the expected number of τ events is 12.8 for $\Delta m^2 = 2.4 \times 10^{-3}$ eV^2 (19.9 for $\Delta m^2 = 3 \times 10^{-3}$ eV^2) while the background expected is less than 1.

In addition to the dominant $\nu_\mu \rightarrow \nu_\tau$ oscillation it is possible that a sub-leading transition involving ν_e occurs as well. Thanks to its excellent electron identification capability, OPERA has the potential to observe the appearance of ν_e if θ_{13} is close to the nuclear reactor limit. In case of no ν_e observation and assuming $\Delta m^2 = 2.5{\times}10^{-3} eV^2$, OPERA will be able to set a limit $\sin^2\theta_{13} < 0.06$ (90% C.L.) [54]

Chapter 3

Nuclear emulsion and European Scanning System

3.1 Brief history of nuclear emulsions

Nuclear emulsions have a long history in high energy physics. Their excellent spatial granularity and resolution (less than 1 μm) make them suitable to detect short lifetime particles.

The use of photographic emulsions to study nuclear particles started in 1896 when H. Becquerel discovered radioactivity by observing for the first time the blackening of photographic plates accidentally in contact with salts of uranium. In 1946 an industral chemist, C. Waller, produced the first "concentrated" emulsions, with a higher halide/gelatin ratio such to make them more sensitive to minimum ionizating particles. In 1947 with this technique C. F. Powell discovered the pion by observing the $\pi \rightarrow \mu$ decay in nuclear emulsions exposed to cosmic rays [55]. In the following years, several particles like the K mesons and hyperons were observed thanks to the usage of detectors based on nuclear emulsions. In the 1960s, accelerators began to replace cosmic rays as sources of high-energy particles, and electronic detectors like counters and spark chambers started to be used for the experiments. However, due to their high resolution, nuclear emulsion were never abandoned and recently have been used in neutrino experiments: E531 [56] at FermiLab aiming at the measure-

ment of charmed particle lifetimes in neutrino interactions; DONUT [5] at FermiLab which performed the first and still unique ν_τ detection, CHORUS [57] at CERN. All these experiments have an hybrid design: electronic detectors predict the emulsion region where to search for neutrino interactions while emulsions act as passive target. Though nuclear emulsions used today are similar to those used 50 years ago, the analysis techniques have changed drastically: actually, the use of large nuclear emulsion detectors has been particularly favoured by the development of automatic scanning systems.

3.2 Basic properties

Nuclear emulsions are made of micro-crystals of silver halides (AgBr) suspended in a gel composed by organic materials. They are similar to photographic emulsions but differ from them in the uniformity, size and sensitivity of the silver halide crystals to detect tracks with good efficiency. The silver to gelatin ratio is much higher than in a conventional emulsion and the thickness is larger too. The linear size of the crystals spaces between 0.1μm and 1 μm.

The passage of charged particles can become visible through a chemical amplification of the atomic-scale perturbations.

If the silver halides are opportunely sensibilized the energy released by ionizing particles to the crystals produces a latent image quite stable in time.

The formation and preservation of the latent image depends on external conditions such as temperature and humidity. As temperature increases, the sensitivity decreases and the latent image becomes less stable (fading). When the emulsion is developed a chemical agent reduces the AgBr crystals to metallic Ag more rapidly than the not irradiated crystals. So when the emulsion is developed the crystals containing the latent image are reduced to metallic Ag while the other crystals are removed by fixing and washing. The result visible at microscope is a series of dark silver grains which identifies the path of an ionizing particle.

The grain density along a track of a particle of well-known charge and velocity de-

pends on the sensitivity of the emulsion and on the development process. Presently nuclear emulsions can be produced with controlled composition (the crystal concentration usually 20%-50% in volume enriched with particular elements). A minimum ionizing particle (mip) yields about 30 grains in 100 μm of emulsion with a diameter of 0.6-0.8 μm.

3.3 OPERA emulsion films

The total area of emulsion sheets in the OPERA experiment is higher with respect to that ones used in the previous experiments: about 150000 m^2 which correspond to about 12 millions of 12×10 cm^2 films. The emulsions used in the past experiments were poured by hand according to standard procedures tested in many years of experience. The same procedure applied to OPERA would have been prohibitive for time consuming. Thus OPERA emulsions have been produced by commercial photographic film machines by Fuji-Film Co. in Japan. The whole pouring and coating process has been established after an extensive R&D project between the company and the Nagoya University. The cross section of an OPERA emulsion film is shown in fig. 3.1. Two emulsion layers of ∼44 μm thickness are coated on both sides of a 205 μm thick triacetate base. In order to prevent the occurrence of black or gray patterns on the emulsion surface, due to silver chemically deposited during the development process, a protective gelatin coating 1 μm thick has been put on the sensitive layers. The presence of this protective coating allows direct contact with the lead plates. In absence of this protection it should have been necessary to insert thin insulator sheets in order to avoid chemical reactions between lead and silver halides contained in emulsions. Unlike hand-made films, the thickness of the emulsion layer can be precisely controlled as in the case of commercial color films. The crystal diameter ditribution in the emulsion layer shown in fig. 3.2 is quite uniform around 0.2 μm.

The background due to the so-called "fog" (see Fig. 3.3), constituted by accidentally developed grains distributed randomly in the emulsion volume, is under control by applying a moderate development to the emulsion films without affecting

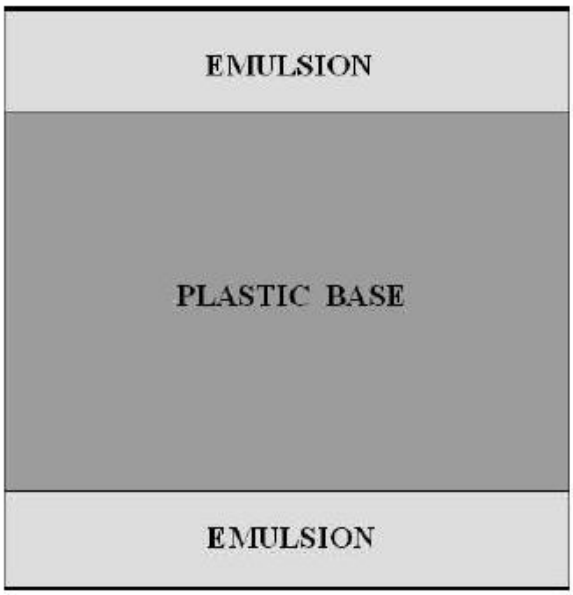

Fig. 3.1: Cross section of a machine-coated OPERA emulsion film

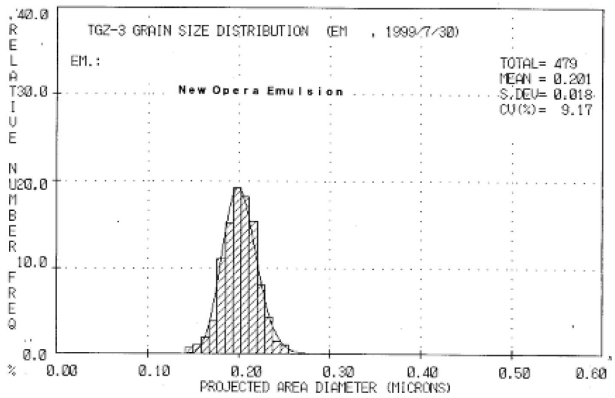

Fig. 3.2: Crystal diameter distribution of the Fuji emulsions produced for the OPERA experiment.

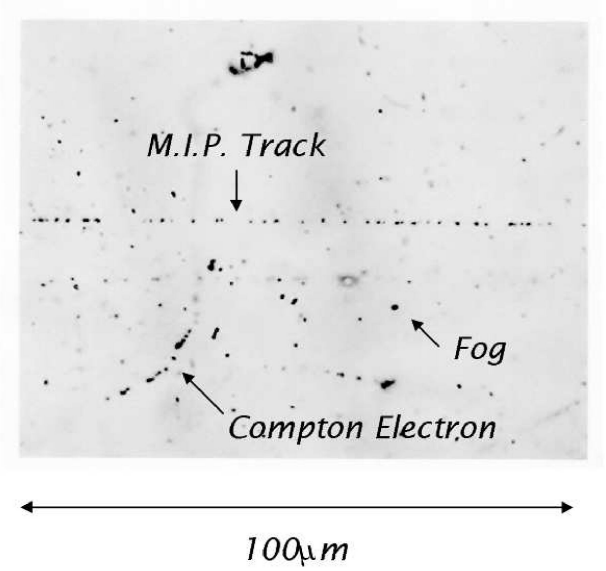

Fig. 3.3: Picture of a minimum ionising particle (mip) recordered in an emulsion layer. The grain density is defined as the number of grains per 100 μm track; the fog density as the number of fog grains per 1000 μm^3.

the sensitivity of $\sim$ 30 grains per 100 μm. The fog is kept at resonable levels ($\leq$ 5 grains/1000 μ^3). This value is also depending on the refreshing procedure.

The intrinsic position resolution of the emulsion films can be investigated through the measurement of the position residuals of the centre of each grain with respect to a fitted straight line as shown in fig. 3.4

The measured resolution of σ $\sim$0.06 μm is compatible with the expected value of $0.2\mu m/\sqrt{12}$ (that is 0.058 μm), where 0.2 μm is the diameter of the original crystal. In the following there are listed some of the basic properties of OPERA emulsions:

- density $\rho = 2.4$ g/cm^3,
- average atomic number $\langle A \rangle = 18.2$,
- average atomic charge $\langle A \rangle = 8.9$,
- radiation length $X_0 = 5.5$ cm,
- $(dE/dx)_{mip} = 1.55$ MeV/g/cm^2 or 37 keV/100 μm,

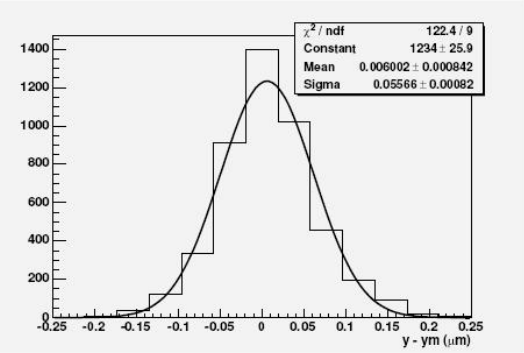

Fig. 3.4: Position residuals of grain centre with respect to the corresponding fitted track.

- nuclear collision length $\lambda_T = 33$ cm.

3.3.1 Emulsion refreshing

OPERA emulsion films production started on April 2003 and up to now about 8 millions of emulsions have been produced and shipped to Gran Sasso Underground Laboratory. Because of their continuous sensitivity, emulsions collect latent track images, from cosmic rays and environment radioactivity since the moment of their "birth" at Fuji firm until their installation in the OPERA detector. In order to erase these tracks an accelerated fading procedure is obtained by keeping emulsion films at a moderate temperature and high humidity for a few days. This procedure, known as $refreshing$ is able to delete the latent tracks with a current efficiency of 98%. After the production, the OPERA films are stored in the Tono mine in Japan, in the refreshing facility at a depth of 96 m. The fill refreshing cycle lasts 1 week and is organized into 3 phases:

- $Pre-humidification$: emulsions are stored at 27° C and moderate humidity (∼60% RH) for 24 hours.
- $Refreshing$: for 3 days emulsions are kept at RH ≈ 85-99% and T ≈ 26-29° C.

- *Drying*: after refreshing films are gradually conditioned to 20° C and 50% RH. This steps last 3 days.

After drying films are packed under vacuum is stacks of 9 ECC basic units and stored underground waiting for the shipment to Gran Sasso. Here, a second refreshing procedure is foreseen only for the Changeable Sheets (CS) in order to delete the cosmic rays tracks collected during the transportation. Without the CS refreshing, the search for neutrino interactions in the area triggered by the electronic detectors wuold be much more time consuming.

The required sensitivity for emulsion films is at least 32 grains/100 μm. Films below this threshold can not be used in the OPERA target.

3.3.2 Emulsion processing

The processing procedure adopted for OPERA films is shown in Tab. 3.1. The entire process lasts about 3 hours. In addition, more other procedures are necessary in order to obtain uniformity of development and minimize the distortion.

The development is the process by which the latent image contained in emulsions is made visible by reducing the silver ions of the halide crystals into metallic silver. For nuclear emulsions a chemical developer is chosen, to reduce completely the crystals containing the latent image centre, leaving unchanged those ones which do not contain any centre. The development time should be enough to reduce completely the crystals with the latent image centre but not so long to develop also the unexposed crystals. Anyway, a certain number of crystals will be developed even if they do not contain a latent image centre. They constitute a background (fog).

Chemical development, like many other chemical reactions depends on temperature: it occurs more rapidly at higher temperatures while below 10° C it stops. It is fundamental, therefore, to keep the processing temperature constant during the development otherwise it will not be possible to estimate the correct development time. The development of OPERA films is performed at 20°.

After the development, a stop bath is foreseen in order to arrest the action of the

Step	Time	Chemical composition (1 liter)
Development	25'	Fuji Developer (PDT) (250 ml) Fuji Starter (RD-90S) (20 ml) Demineralized Water (750 ml)
Stop	10'	Aluminun Sulphate (8.5 g) Acetic Acid pure(5 ml) Demineralized Water (1 l)
Clean	10'	Demineralized Water (1 l)
Fixation	35'	Fuji Fixer (UR-F1) (500 ml) Water (500 ml)
Washing	4x20'	Circulating Water
Glycerin + Driwell	20'	Glycerin (200 ml) Fuji Driwell (5 ml) Water (800 ml)
	1"	Fuji Driwell (5ml) Water

Tab. 3.1: OPERA emulsion processing final procedure.

agent deveoper. A fixing procedure follows to remove all the residual silver halides, leaving the metallic silver to form the image. If these residual halides are left in the emulsion they would slowly induce the browning and the degradation of the image. The fixing agents more used are sodium or ammonium thosulphate, which form thiosulphate complexes with the silver halide.

In order to preserve the fixer solution and guarantee more stability in emulsion quality, a clean bath of pure water between stop and fix is foreseen.

After the fixation the emulsion must be washed very thoroughly, to remove all the silver thiosulphate complexes in the emulsion. If any do remain, they will eventually break down, forming silver sulphide which is brown and will obscure the image. It has been decided to have a long washing procedure to ensure emulsion transparency and long term stability.

Hence, a bath of alchol and glycerin is used to have a stable thickness for films of about 44 μm and a fast driwell immersion to avoid the occurrence of drops on emulsion surface. These two steps have been introduced to guarantee a uniform

emulsion thickness and surface planarity for fast micorscope scanning.

Due to organization and manpower reasons, it is planned to distribute the bricks extracted in a week over 5 working days of development.

The films to be developed per day will correspond to about 42 bricks (84 CS underground + about 2400 films at surface); so the entire development procedure for OPERA emulsions has been commissioned to automatic emulsion handling chains.

3.4 Processed emulsions

The possibility to obtain a tracking precision less than 1 μm depends on the stability of grain relative positions inside emulsion during and after the development. We have to take into account two main deformation effects: the *shrinkage* and the *distortion*.

Shrinkage effect After processing, an emulsion will occupy less volume than before unless some material is added to replace the silver halides dissolved during the fixing. The evidence of this effect is a reduction of the emulsion thickness (*shrinkage*). We may define the "shrinkage factor" as the ratio between the emulsion thickness at the exposure time and the thickness after development.

Both gelatin and glycerin are hygroscopic so that the effective equilibrium thickness is depending on the environment humidity. Processed emulsions change their thickness with the environment humidity in the way that when the humidity is near 60% is

$$\frac{\Delta t}{t} \cong \frac{RH^2}{3 \cdot 10^4} \tag{3.1}$$

where t is the nominal thickness, Δt is the increase from the dry thickness and RH is the relative humidity in per cent. The shrinkage factor must be taken into account in the tracking algorithm because the measured track slope must be multiplied by this factor to obtain the real value. The effect is shown in fig. 3.5.

Distortion The distortion is a local deformation of the emulsion surface which limits the precision of measurement on tracks. Distortions can change from one

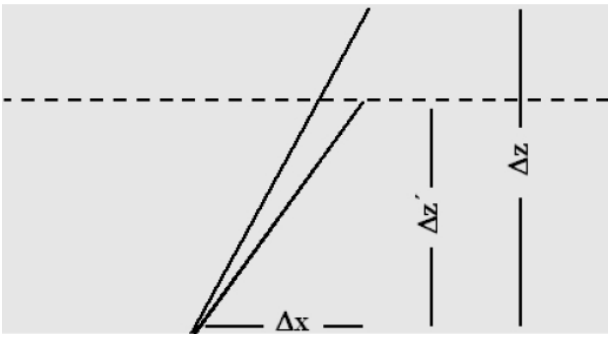

Fig. 3.5: The shrinkage effect: the measured track slope $\Delta z'/\Delta x$ does not coincide with the real slope $\Delta z/\Delta x$. The correction is obtained by multiplying the measured slope by the shrinkage factor $\Delta z/\Delta z'$.

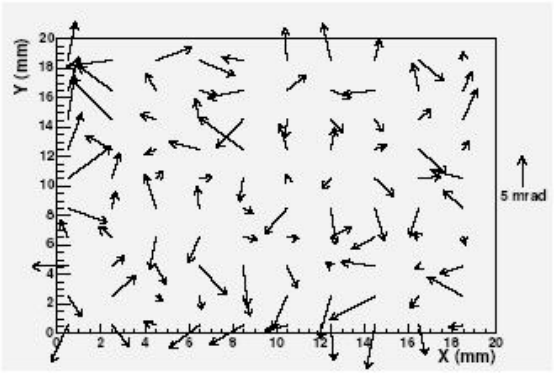

Fig. 3.6: Map of a typical distortion distribution of an OPERA emulsion

region of the emulsion film to another, but but can be considered as constant over the order of 1 cm^2. A typical distortion map measured in a OPERA emulsion is shown in fig. 3.6. The arrows indicate the direction of the distortion while the length of the arrow indicates its absolute value. The average value of the measured distortion is $\sim$ 5 mrad.

The use of a double layer emulsion coated on a plastic support improves the angular resolution at a level of 2 mrad. The track direction can be defined by the two points in proximity of the plastic base which are considered free from distortions.

3.4.1 Fading

The latent image of a particle track gradually fades after exposure (fading), so if the emulsion is leaved unprocessed, the developed grain density will be smaller as the time between exposure and processing increases. This effect in more rapid in emulsions with small grain size, and for emulsions kept at high temperature and/or humidity.

Fading is not a severe problem in OPERA experiment since it is planned to extract the candidate bricks and develop emulsions within one week after the event occurring. It is possible to take advantage of the existence of some fading, whose contribute erases undesired cosmic ray tracks collected during film production and transportation before the run.

Several tests on sensitivity have been done to check the features of Fuji emulsions [58]. In November 2004, a stack of 80 not refreshed emulsions was exposed at CERN horizontally to a 8 GeV pion beam. After the exposure, emulsions were packed at about 20° C temperature and different humidities, and developed at different times within a week. Hence each emulsion has been single-packed and stored at 20° C and 60% RH. The results show (see fig. 3.7) that the erasing rate is strongly dependent on humidity.

It has been possible to evaluate emulsions fading ratio measuring a reference sample after 1 month storage at 20° C and 50% RH: the measured Grain Density is 26.2 ± 1.5 grains/100μm, lower of 12.5% with respect to the standard value 30 grains/100μm. This result is very important to understand the best conditions for OPERA emulsions storage. The behavior of the reference sample is also reported in fig. 3.7.

3.5 The automatic scanning system for emulsions

A large scale experiment like OPERA, which uses a big amount of nuclear emulsions is possible thanks to the improvements of emulsion techniques during the last two decades as well as the development of very fast automatic scanning systems.

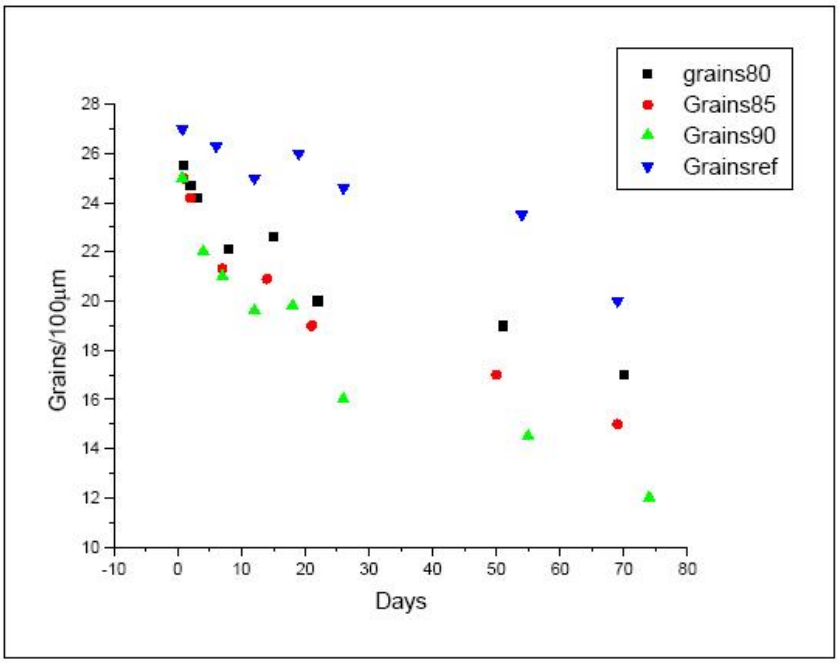

Fig. 3.7: Grain Density counting over OPERA emulsion samples stored at 20° C temperature and different RH: 80% (black), 85% (red) 90% (green), 50% (blue).

The prototype of an automatic scanning system to analize emulsions consists of a microscope with a motor driven stage, a dedicated optical system, a digital camera (CCD or CMOS) for image grabbing connected to a vision processor, a motor control board. The emulsion scanning is done by microscope with a vertical resolution of few microns: by adjusting the focal plane of the ojective the whole emulsion thickness is crossed and a sequence of tomographic images of each field of view is taken at different depth (every $2 \div 3$ μm) in the emulsion. These images are processed, and sent to the vision processor board, and analyzed in order to reconstruct the three-dimensional structure of the tracks.

The first completely automatic scanning system, the *Track Selector* (TS) has been developed at Nagoya University. The TS and the improved version UTS (Ultra Track Selector), have been successfully used in CHORUS and DONUT experiments.

The scanning speed required in OPERA is about 20 cm^2/hour. In order to get

this aim two different *R&D* programs have been carried out: the Nagoya group, aiming to further improvements to the UTS (the so called Super UTS) and the European Collaboration which cooperated to realize the *European Scanning System* (ESS).

3.6 European Scanning System

The ESS consists of a rigid table used as support, a granite arm, a motor driven scanning stage for horizontal (XY) motion, a motor driven stage mounted vertically (Z motion) on the granit arm for focusing, an optical system and a digital camera (CCD or CMOS) for image grabbing both fixed to the granit arm; a vision processor board in the host PC, an illuminating system under the scanning table. The emulsion sheet is placed on a glass plate and is held during the scanning by a vacuum system which guarantees its flatness. The specifics of the European Scanning System follow these requirements:

- high performance mechanics with sub micro-metric accuracy in position for both horiziontal and vertical stage, with a small settling time in the motion from one field of view to the next one (less than 0.1 s);
- camera 1280×1024 pixels with a high frame rate (greater than 350 frame/sec);
- optical system with a large field of view (390×310 μm^2), and a 50X magnification objective[1] in order to have $\sim$ 4 pixels for an object of the order of the processed grain size (0.8 μm);
- powerful image processors.

A prototype of one of the Bologna ESS is showed in fig. 3.8.

[1]Due to a custom modification of the optical distance from the camera this objective acts as 40×

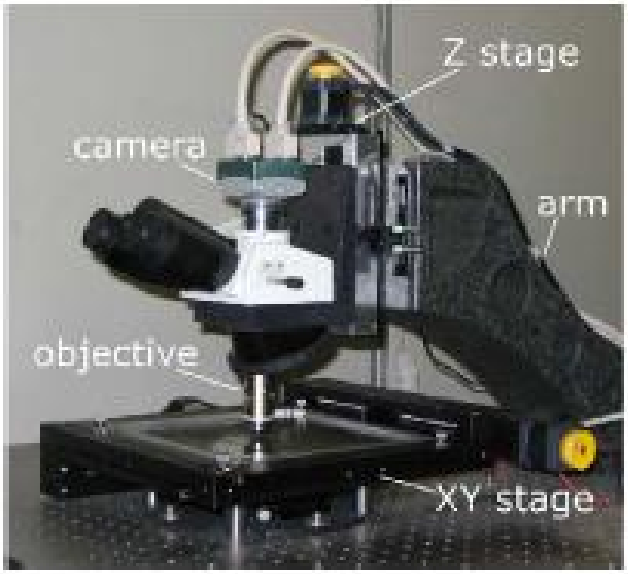

Fig. 3.8: A picture of a microscope of the European Scanning System in Bologna

3.6.1 Mechanics: the stages

The scanning table as well as the vertical stage have been developed together with Micos company[2], by modifying the commercial products acording with the OPERA requirements. The stages are equipped with stepping motors produced by Oriental Motor[3], and are controlled by the FlexMotion board by National Instruments hosted in the PC. The scanning table of the ESS has a range of 20.5 cm in both horizontal directions (XY) and the coordinates are read out by two linear encoders with 0.1 μm resolution. Limit switches are integrated on each axis.

The horizontal motion speed is a crucial point to obtain : it is fundamental to set parameters as maximum speed, acceleration and time profile in order to minimize the time needed to change field of view. The size of horizontal displacement between consecutive fields of view fixed by the camera sensor size, by the optical magnification and by the necessary superimposition of the field is 360 μm along X direction and

[2]MICOS ITALIA GmbH, via S. Protaso, 39 I-20010 Bareggio MI
[3]http://www.orientalmotor.it

280 μm along Y direction.

The total time to move from one field of view to another is obtained by the sum of the *rise time* and the *settling time*. The first is the time needed to reach the "target point" while the second is necessary for waiting for the oscillations which have to be dampened at a reasonable level ($\pm$ 0.2 μm) corresponding to a value smaller than one image pixel (0.3 μm). Even though the acceleration and speed parameter are set to the same value for both XY axes, they behave in different ways: the X axis concludes the displacement in $\sim$ 100 ms while the Y motion can be considered concluded within $\sim$ 140 ms: this is due to the fact that the Y motions involve the entire table while the X motions involve only a light part of it. For this reason the scanning procedure minimizes the number of Y displacements.

The vertical stage (Z axis) is equipped with a linear encoder of 0.05 μm resolution as well as an integrated limit switch. During the data acquisition, the vertical stage moves at a constant speed in order to take equally spaced images of the emulsion. The speed is calculated taking into account the camera frame rate, the number of frames to be taken and the emulsion thickness: with a frame rate of about 377 frames per second and 15 frames to grab, each image is acquired at a relative distance of about 3 μm (the emulsion thickness is 44 μm), so the resulting speed is around 1150 μm/s and the time to scan a field of view in an emulsion side is about 55 ms.

3.6.2 Optics

The optical system (objective + lens tube), must satisfy the scanning requests in terms of quality and resolution: it is necessary an image focusing at different depths and a magnification of few pixels per micron. The objective is designed so that light emerging from the rear aperture is focused to infinity optics. A second tube lens hosted in the trinocular forms the image at its focal plane.

Given the total thickness of the emulsion including the plastic base the requested *Working Distance* (W.D.) in order to see the backside of the emulsion is $>$ 0.3 mm, while the *Numerical Aperure* (N.A.) must be larger than 0.8 to get sub-micrometric resolution. In order to minimize the spherical aberrations which increase as the

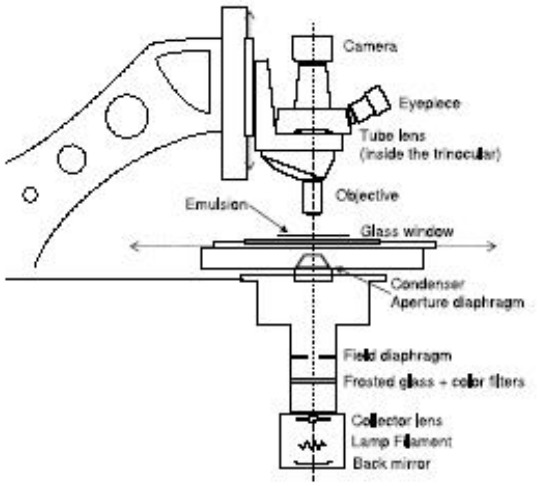

Fig. 3.9: Schematic layout of the of optical system of an ESS microscope

cube of N.A. the variation of the intermediate medium between the focal plane and objective must be small. An oil immersion objective has been chosen, since this kind of oil has a refractive index (1.51) very similar to the emulsion ($\sim$ 1.51) and to the plastic base one ($\sim$ 1.48), so that light passing the emulsion encounters a medium homogeneous optically . Images from the objective crossing the trinocular tube reach the camera sensor.

3.6.3 The camera and the Vision processor

The camera used in the ESS is a MC1310 Mikrotron[4], with high frame rate and megapixel resolution and provided of a Full Camera Link interface. The sensor has 1280 $\times$ 1024 pixels and the can work at the maximum rate of more than 500 frames per second (fps). The configuration which allows to reach the desired scanning speed (20 cm^2/h) is 377 fps.

The images are grabbed in a 256 gray level scale (the light acquired by a single pixel is converted into a digital 8-bit signal) and are sent to the frame grabber hosted in the PC. The frame grabber and the image processor are integrated in

[4]Mikrotron GmbH, landshuter Str.20-22 D-85716 Unterschleissheim (Germany)

the same board, the Matrox Odyssey Xpro[5], specifically designed for onboard image processing at high speed. The processor is a Motorola G4 PowerPC equipped with a DDR SDRAM memory (1 GB). A Full Camera link connection allows an acquisition rate from the camera of up to 680 MB/s. A rate of 377 fps and 8 bit gray level images correspond to an acquisition camera rate of 471 MB/s. The acquisition time for each field of view of emulsion taking account of its thickness is about 40 ms.

3.6.4 The illumination

The illumination system developed by Nikon-Italy cooperation, is located under the scanning table and works in the Koehler configuration [59]. The light from the lamphouse is directed into the microscope base by means of a lens (collector), and then through a glass diffusor, to be focused on the aperture diaphragm of a condenser placed below the stage, which concentrates the light into a cone to illuminate the emulsion. a second diaphragm called field diaphragm, is adjusted to avoid that emulsion can be illuminated or heated outside the field of view.

The numerical aperture of the condenser should match that of the objective in order to get a wide illumination cone and a high optical resolution. The condenser used is a Nikon achromatic with N.A. = 0.8 and W.D. = 4.6 mm compatible with the requirements of the glass plate which holds the emulsion, whose thickness is 4 mm. A glass diffusor as well as a green filter, can be used to obtain a uniform illumination and a high optical resolution.

3.7 The online DAQ

The software for on-line track reconstruction of the emulsions, developed in C++ language has a modular structure accessible through a window panel from which it is possible to control the configurations and settings of the objects, each one with a specific task shown in the Tab. 3.2

[5]Matrox Electronic Systems Ltd., 1055 St. Regis Blvd., Dorval, Quebec (Canada)

Module	Function
Objective	stores the information related to the used objective and performs the pixel to micron conversion
Odyssey2	pilotes the Odyssey board
FlexStage4	is interfaced to the stage controllers and sets the motion
SmartTracker7	performs the track pattern recognition, recognizing sequences of geometrically aligned clusters.
SmartFitter	performs the tracks fit.
DataIO	handles the Input/Output of data.
SheetMap2	transforms coordinates and vectors from the current stage reference frame to the emulsion local reference system defined by a grid of fiducial marks printed on the emulsions).
VertigoScan5	is the steering module, which uses all the other objects to control the scanning and its parameters

Tab. 3.2: List of the modules of the on-line acquisition software.

The output data format is a collection of raw binary data which will be saved into an Oracle DataBase structure developed for storage. The images are grabbed and digitised into 256 gray level scale where 0 corresponds to black and 256 to white, then sent to the Matrox board for cluster searching. Some clusters are track grains while the most part constitute the fog.

The first important step is the $flat\ field$ subtraction. It consists of an image grabbed outside the emulsion which will be later subtracted from the image inside. Its clusters are dark spots essentially due to dusty residuals on the camera that would lead to the reconstruction of vertical fake tracks, and have to be removed. Often, the image of emulsion is not very clear because of shadows presence due to grains which are not focused, or potential defects like scratches and dirt. Hence, the further operation is the "image filtering" in order to enhance the constrast of dark spots (focused grains) on the lighter background. The filtering is realized by applying a convolution filter: each pixel output value is the result of a weighted sum including the neighborhood pixels of input value. The weights are given by the

convolution kernel.

At this point a well-chosen threshold is applied to extract the dark spots candidate to be grains: the pixels with the filter response below the threshold whose values in binarized image are set to 0 are the white pixels while those ones which exceed the threshold (value set to 1 in binarized image) are classified as black. From the choice of kernel and threshold depends the effective focal depth of the system which is for the ESS, tipically about 2.5 μm.

The further step is an "equalization" procedure applied to the image in order to have an homogeneous distribution of clusters inside the grabbed frames. It is based on the definition of several cells, scanning the related emulsion surface and counting the number of detected clusters for cell according to different threshold applied.

The last step of image processing is the so called "clusterization": the image is scanned row by row searching for sequences of black pixels to be merged in clusters. It two or more clusters come into contact they are also merged. A reasonable cut depending on the illumination,on processing parameters and on cluster areas, helps to reject the background caused by the noise in the camera signal.

Finally, position, area and shape of clusters are calculated and given in the output results.

3.7.1 Tracking

The next step, uses the previous informations to combine clusters from different layers in order to perform the recognition of geometrical alignments and then reconstruct the so called *microtracks*. This is the first part of the tracking algorithm. The second phase is the track fitting which performs a linear fit of the position of the clusters and evaluates tracks slopes. Intercepts are given on the surfaces between emulsion layers and plastic base.

All the operations are real time according to the time requested for image processing and for the mechanical motion.

The field of view is subdivided in cells about 25 μm wide in order to reduce the

CPU time. Usually, 1000-2000 clusters, almost due to random background are found in a field of view. By applying quality cuts it is possible to select a 60% of them to be used for tracking. The first step is the trigger search: the layers are enumered and some *layer sequences* are defined. Each sequence is formed by one layer of the emulsion top side and another one of the bottom side, plus some inner layers.

The requested alignment tolerance and the number of layers to use depend on the features of the emulsion and on the quality of the track to search.

In each sequence, the lines joining a couple of clusters belonging to the top and bottom layers are considered, around them a volume in acceptance is built. Looking in the inner layers of the sequences, if in the volume at least one cluster is found, then a trigger signal is generated. When a start up track is found, the track is followed in all the others layers. Also the neighbour cells are investigated for the track following, in order to increase the angular acceptance. In each frame the acceptance area is an ellipse with the minor semiaxis representing the transverse resolution and the major semiaxis representing the longitudinal resolution.

All clusters found inside the same acceptance volume are assigned to the same microtrack. If the clusters number exceeds a defined threshold, the sequence is passed to the fitting part od the algorithm. Usually not all track slopes are physically interesting so an angular acceptance given by $\tan\theta < 1$ is fixed (θ is the angle between the track direction and the vertical direction).

Moreover, taking into account that with an emulsion sensitivity of 31 grains per 100 μm for a m.i.p. track, the number of grains in one emulsion side (44 μm) is about 13, microtracks with less than 6 grains are discarded. After finding all clusters belonging to each microtrack a bidimensional linear fit is performed. After this, the informations related to the microtrack slope, the intercept, the number of clusters and its resolution are stored in the raw data output file.

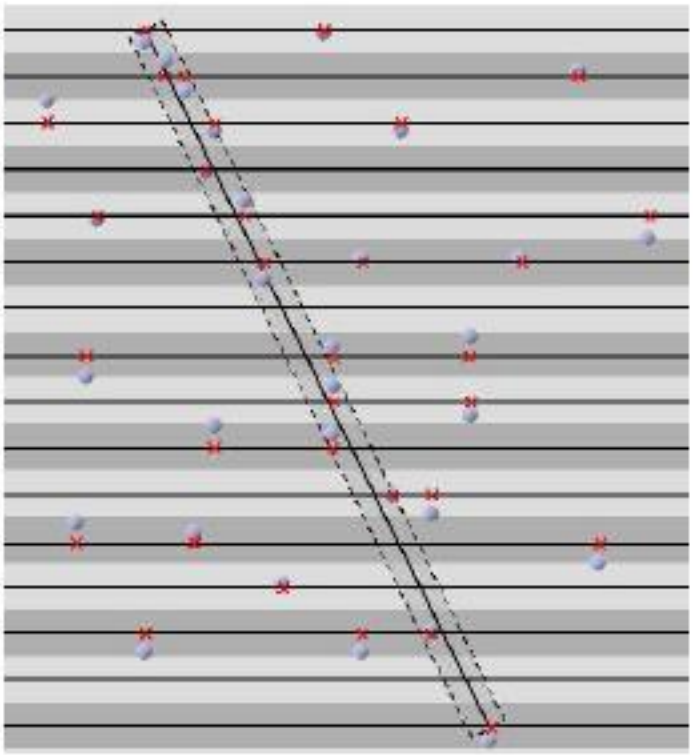

Fig. 3.10: A schematic view of the tracking. Horizontal gray strips individuate the focal planes, while horizontal black lines represent the corresponding Z coordinates. The crosses individuate the cluster positions. The dotted area shows the acceptance volume and includes the fitted track.

3.8 Track reconstruction in the emulsion

The on-line DAQ software stops at the microtracks reconstruction. The next steps are performed by an off-line algorithm for the track reconstruction. It is developed in the following steps:

- linking of microtracks to obtain the basetrack
- plate to plate alignment
- volume track reconstruction

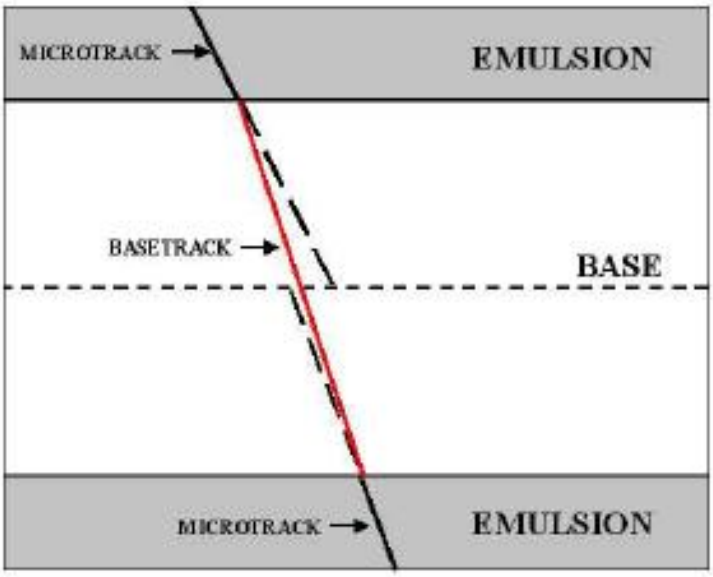

Fig. 3.11: Scheme of basetrack reconstruction.The matching of the microtracks is obtained within an acceptable agreement in position and slope. The basetrack is formed by joining the two points closer to the base.

Linking The basetrack is obtained by connecting two microtracks through the plastic support. The volume track is formed by at least two basetracks in different emulsion sheets. In this way it is possible to reconstruct the trajectory of a particle crossing a whole brick.

The basetrack reconstruction is performed by the projection of two microtracks across the plastic base and the search for an agreement within slope and position tolerances consistent with the expected angles and position resolution (see fig. 3.11).

The basetrack is defined from the join of the intersection points of the two microtracks with the measured surface of the plastic base. The angular difference between microtrack and basetrack provides an estimation of the microtrack angular resolution.

Basetracks are also selected on the basis of a quality estimator of the microtracks angular agreement defined in the following way:

$$\chi^2 = \frac{1}{4}\left[\frac{(\theta_{xt}-\theta_{xB})^2}{\sigma_x} + \frac{(\theta_{xb}-\theta_{xB})^2}{\sigma_x} + \frac{(\theta_{yt}-\theta_{yB})^2}{\sigma_y} + \frac{(\theta_{yb}-\theta_{yB})^2}{\sigma_y}\right] \tag{3.2}$$

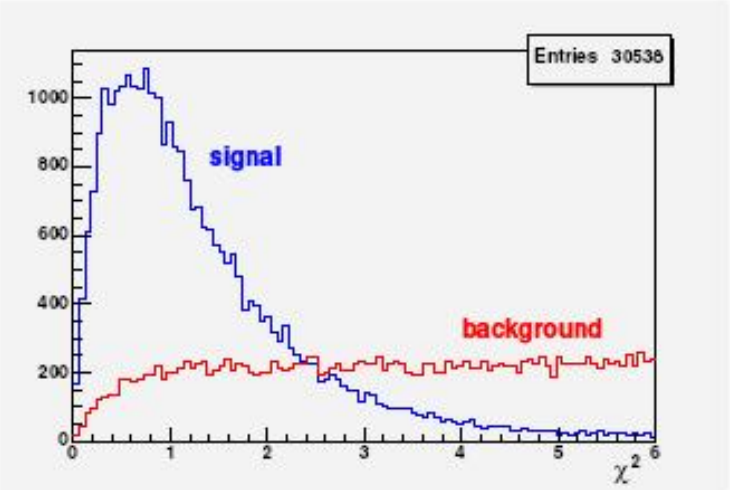

Fig. 3.12: χ^2 distribution for basetracks. The background is due to the alignment of fog grains randomly distributed.

where $\theta_{xt(b)}$ and $\theta_{yt(b)}$ are the projections of the top (t) and bottom (b) micro-track angles in the $z-x$ plane and $z-y$ plane, θ_{xB} and θ_{yB} are the same projections for the base-tracks (B) and σ_x and σ_y are the micro-tracks angular resolutions. A typical χ^2 distribution is showed in fig. 3.12.

Plate to plate alignment

In OPERA, the candidate brick removed, is carried to a location at a depth outside the underground hall, to be exposed to the cosmic muon flux. This provides a pattern for the alignment between consecutive emulsion sheets inside the brick.

The plate to plate alignment is performed by the algorithm by dividing the emulsion sheets in several cells and for each cell a pattern recognition is done between the basetracks of two consecutive sheets. While one pattern is kept fixed, the other is shifted with many displacements till when the maximum number of track coincidences is found.

The resulting alignment pattern is described by the affine transformation:

$$\begin{pmatrix} x' \\ y' \end{pmatrix} = \begin{pmatrix} a_{11} & a_{12} \\ a_{21} & a_{22} \end{pmatrix} \begin{pmatrix} x \\ y \end{pmatrix} + \begin{pmatrix} b_1 \\ b_2 \end{pmatrix} \tag{3.3}$$

The alignment is better when performed on a local surface of the emulsion sheets in order to minimize the effect of global deformation of the films. The required track density of cosmic muons for an accurate sheet to sheet alignment is about 1-2 tracks/mm^2.

Volume track

After the alignment procedure, the algorithm performs the volume track construction based on finding and fitting a sequence of basetracks (at least two). The basic principle is the connection of pairs of basetracks, trying to extend them in both directions inside the brick. In this way a basetrack chain forming the volume track is created. This chain can be arrested in case of some algorithm inefficiency in finding basetracks or when an interaction or a decay is found. The fitting algorithm is based on the Kalman filter.

3.9 Microscope performances

In order to study and maximize the microscope performances, a test beam exposure has been performed in June 2004 at CERN. The goal was to estimate the angular resolution, the tracking efficiency and purity and determine the scanning speed. To this aim a brick without lead (called reference brick) with 64 Fuji emulsions was assembled and exposed to a 10 GeV pion beam at different angles. After exposure each sheet has been scanned according to the on-line procedure by chosing a distance between two consecutive layers of $\sim$3 μm obtained form the ratio between the emulsion layer thickness (44 μm) and the number of active layers (15) as described in the previous section. In fig. 3.13 the angular differences between microtracks and basetracks are showed. As we can see the angular resolution is 9 mrad and 22 mrad respectively for angles θ=0 and θ= 400 mrad.

Using the estimator χ^2 a quality cut has been applied to discard the basetracks with large χ^2 and a small number of clusters (PH) defined below:

$$\chi^2 \leq 0.25 \cdot PH - 3 \tag{3.4}$$

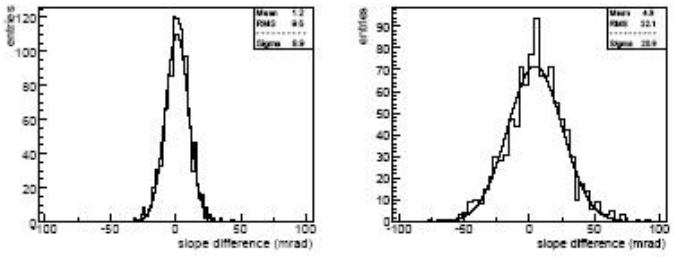

Fig. 3.13: Angular residual distributions between microtracks and basetracks for θ =0 (left) and for θ = 0.4 rad (right)

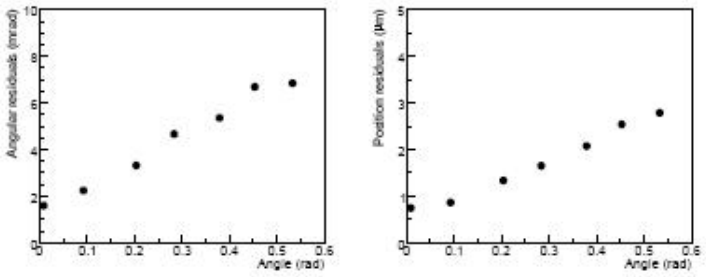

Fig. 3.14: On the left: angular resolution between basetracks and volume tracks as a function of reconstructed angle. On the right: Position resolution of basetracks.

The volume tracks have been reconstructed with the basetracks passing this quality cut. Hence, basetracks angular and position resolutions have been calculated with respect to the fitted volume tracks as showed in fig. 3.14. These differences range from 1.6 to 7 mrad in angle and from 0.9 to 2.5 μm in position for an angular interval [0,600] mrad. The angular resolution of basetracks are one magnitude order better than microtracks resolution affected by the emulsion distortions and shrinkage effects. The tracking efficiency has been evaluated after plate to plate alignment and volume tracks reconstruction in the overall brick. The efficiency of one emulsion sheet has been defined as the ratio between the number of *passing through* volume tracks that cross that sheet and the total number of *passing through* volume tracks. The found efficiency is greater than 90% and corresponds to a microtrack efficiency of about 95%. The tracking purity is given by the ratio between background and signal.

The background in OPERA is constituted by two main sources: the instrumental and physical background. The first is due to random coincidences of two microtracks generated by a random combination of fog grains (fake basetrack). The second is due to any kind of physical source different from neutrino interactions. For the purity evaluation, only the instrumental background has been taken into account. The background estimation has been done on a sample of not exposed emulsion sheets which have been immediately developed after the refreshing. The selection criteria of basetracks were the same used for the exposed emulsions and allowed to reduce the instrumental background to the level of 2 fake basetrack/cm^2 within an angle of 400 mrad. Since the summer 2004 the ESS has reached the planned speed of 20 cm^2/h per 44 μm of emulsion layer thickness. About 20 ESS microscopes have been installed in the European laboratories of the OPERA collaboration. More than five at Gran Sasso for the CS scanning.

Chapter 4

Algorithms for the analysis of neutrino interactions in the ECC

In OPERA, once that the procedure of the event reconstruction with electronic detectors is completed, the candidate brick is extracted, scanned and analysed, in order search and confirm the products of the neutrino interaction. The procedures for the localization and reconstruction of the interactions in ECC are being pointed out by the collaboration and in this chapter we perform an attempt to study and optimize the algorithms which perform the event reconstruction using MC simulations. In the following I shall provide a general description of the procedure adopted for the OPERA emulsions analysis. Then, I will describe the MC data sample adopted, the algorithms developed, and their performances on the simulated data. Hence the analysis and the results are shown.

4.1 OPERA emulsion analysis and event reconstruction strategy

The first step before unpacking the brick, is to apply a specific procedure in order to recover the correct alignment between the two Changeable Sheets, needed for the event reconstruction in the emulsions. The brick is so exposed to a strongly collimated X-ray beam. The beam is going to enter the brick from CS1 (the CS

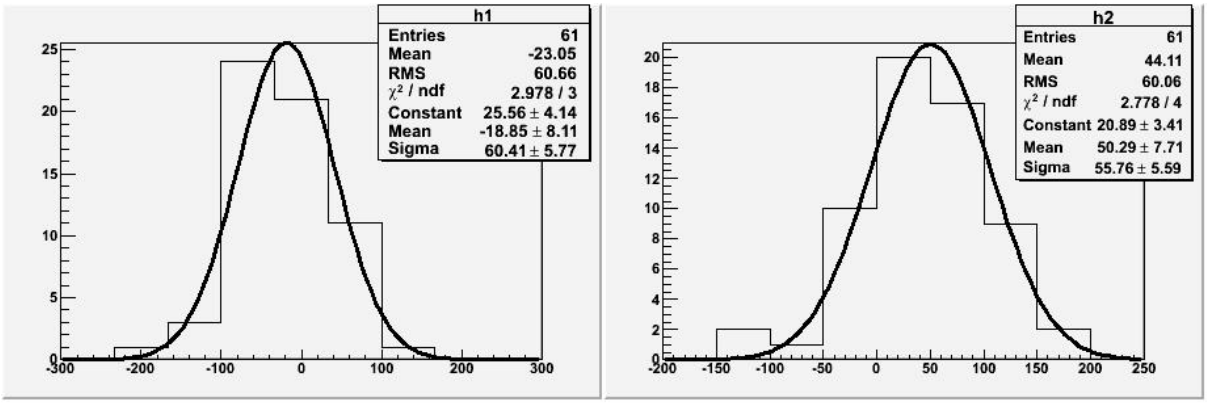

Fig. 4.1: CS to brick position accuracy in X (left) and Y (right)

most downstream the brick with respect to the neutrino beam direction), cross the CS2, the first emulsion plate of the brick closer to the CS doublet till to be completely absorbed while crossing the first lead plate. In this way it is possible to recover the alignment between the two films of the CS doublet with a residual displacement of few μm and between the CS doublet and the brick with a residual displacement of $\sim$50μm (see fig. 4.1). Anyway, further tests are in progress about this topic.

After detaching the CS doublet, the brick is exposed to cosmic rays to guarantee an accurate alignment among emulsion sheets. At this point the process of data acquisition and brick analysis can begin. The procedure consists of two parts: one performed *on-line* and one off-*line*. The *on-line* starts with the emulsion scanning and finishes with the localizazion of the "interaction" points. This procedure is semi-automatic and DataBase-driven. The off-*line* is devolved to the reconstruction of the event topology and to the data analysis.

4.1.1 Changeable Sheets analysis

The first step is the CS doublet analysis: the CS1 is scanned according to the procedure called *general scan*: all tracks with any angle in the range [0,600] mrad are read out in the given scanning area. Electronic detectors provide the predictions in position and angle of the neutrino interaction inside the brick (with an accuracy

of ∼1 cm for CC events). These informations are stored into a scanning DataBase accessible to all the scanning laboratories. Hence the general scan is performed also on CS2.

Tracks found on CS1 will be matched with those found on CS2 within specific position and angular tolerances. If only one candidate is found it is selected as the best candidate. If more than one candidate is found, a selection is made on the best position agreement between the candidates and the predicted basetrack. If no candidate is found it may be due to a fake basetrack selected in the CS1 or to some inefficiency in the CS2.

The tracks matching is done after mapping CS1 on CS2 without performing the plate to plate alignment. At this level the alignment precision given by the X-rays marks is crucial to reduce random coincidences and avoid false candidates to follow.

4.1.2 The Scan Back procedure

Starting from the predictions provided by the CS doublet, a prediction scan starts in the first emulsion plate in the brick (the most downstream plate close to the CS doublet).

First of all a preliminary plate intercalibration is done acquiring the fiducial grid and three small zones, and following the long cosmic tracks selected. This procedure takes several minutes per plate so an adeguate track density (∼2 tracks/mm^2) is needed to make it faster. The intercalibration provides the affine transformation parameters used to follow the selected predictions across the brick, unifying the coordinate system (referred to the first emulsion plate).

The prediction scanning area is tipically 1 field of view around each prediction. The selected predictions will be followed along the whole ECC within angular and position tolerances user defined. Intercalibration and prediction scan phases, will be alterned during the whole scanning procedure. A track will be searched for two more plates before declaring it *stop*. Generally a track stops because a vertex is generated in the next plate upstream or because of a large angle scattering. The

track stopping could be also due to some inefficiency in the emulsions or to some random background basetracks within the tolerances. All this procedure is called *Scan Back*.

4.1.3 TotalScan

Once individuated the *stopping points*, a fiducial volume of few squared millimeters× a given number of plates is open around each of them. The volume is general scanned in order to perform the event reconstruction and confirm the presence of the neutrino interaction. The volume size is chosen such to minimize the scanning time keeping a high efficiency in the event reconstruction.

4.2 Monte Carlo simulation

A MC simulation has been done to study and analyse data from the PEANUT test experiment performed at Fermilab in 2005. In this test, a mini-detector designed similar to OPERA, has been exposed to the NuMI ν_μ beam line in the Hall of MINOS Near Detector (1 km downstream from the source). The beam energy was tuned in low configuration with a peak of ∼3 GeV as shown in fig. 4.2.

The detector, consists of an alluminium structure, made of 4 small walls, each one filled with a matrix 3 (horizontal)×4 (vertical) bricks. The downstream surface of each mini-wall is covered with two orthogonal X-Y planes of scintillating fibers (SFT) for tracking reconstruction. To solve the ambiguity in spatial coordinates, the structure is equipped with two fiber planes U and V oriented at 45° with respect to the X-Y planes. Fig. 4.3 shows a schematic layout (side view) of the apparatus. The Fig. 4.4 shows the front view. For the details of the test beam set-up and exposure see [60].

The simulation of the brick exposure has been done inside the OpRoot framework, the official package of the OPERA experiment. We used the GEANT3 generator implemented inside OpRoot for the transport and interactions of particles and all charged particles hits having a kinetic energy greater than 1 MeV have been

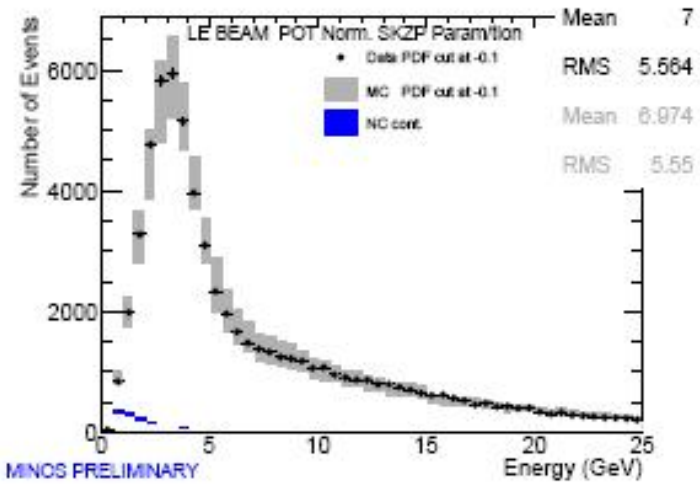

Fig. 4.2: Near Detector Netrino Energy spectrum.

stored. This generator also provides for the basic information at level of microtrack, each one has a well defined slope and intercept with respect to the brick reference frame.

The simulation chain loads these microtracks and on the basis of user defined parameters, apply a recontruction efficiency, an angular and position smearing and simulates the number of clusters per microtrack. The last step of the chain is the microtrack linking and basetrack reconstruction. The package generates output files with the same format of real data.

The MC simulation consists of 5000 neutrino interactions inside each brick of the walls, for each kind of scattering: DIS, QE, RES. The tracking efficiency inserted is ∼78% as real data. This is mainly due to the quality of the emulsions which is rather different to those used for previous tests. No misalignement between emulsion plates has been included. SFT simulation has been included with a track matching efficiency of 80%, without taking account of misalignments with the bricks. Neither cosmic rays nor environmental background tracks have been simulated. The contribution of background to the analysis will be evaluated in a further step.

Fig. 4.5 and 4.6 show the energy distributions and the expected multiplicity for

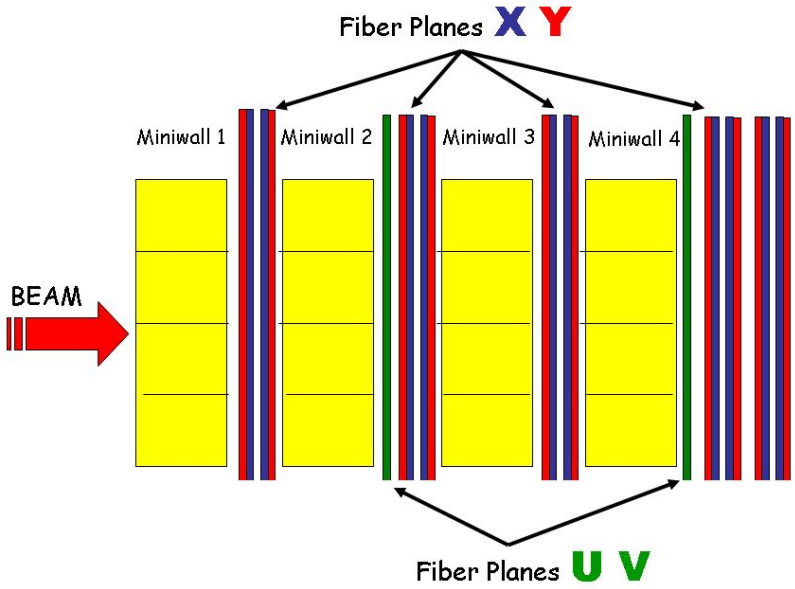

Fig. 4.3: Peanut detector schematic layout: side view. The neutrino beam enters from the left.

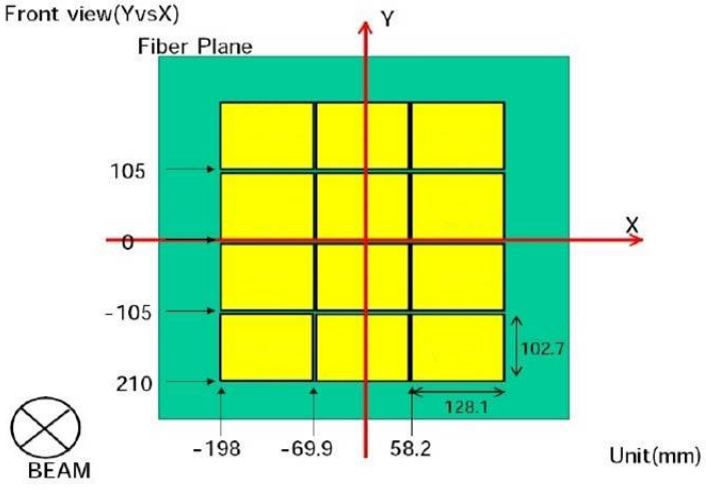

Fig. 4.4: Peanut detector schematic layout: front view

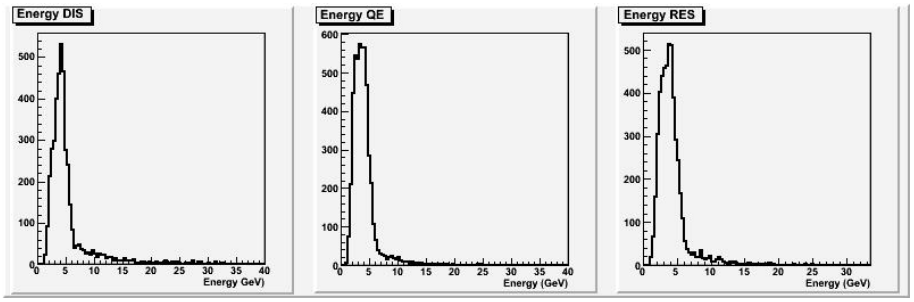

Fig. 4.5: Neutrino interacting energy distributions for the DIS,QE,RES events

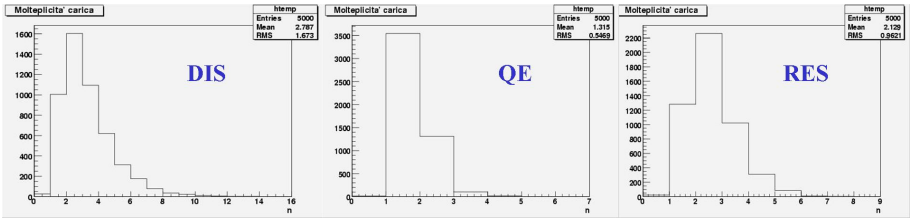

Fig. 4.6: Expected charged particle multiplicity in DIS (left), QE (center), RES (right) ν_μ interactions

the three kind of simulated events.

By folding the distributions of the expected fractions of DIS, RES, QE versus the neutrino energy ranged between 0 and 10 GeV, with the NuMi energy spectrum we estimated the fractions of the three samples:

$$64.4 \pm 0.5 \quad (stat) \pm 1.2 \quad (sys) \qquad DIS \tag{4.1}$$

$$22.5 \pm 0.4 \quad (stat) \pm 0.6 \quad (sys) \qquad QE \tag{4.2}$$

$$13.1 \pm 0.3 \quad (stat) \pm 0.3 \quad (sys) \qquad RES \tag{4.3}$$

4.3 Analysis

4.3.1 Sample selection

The algorithms have been developed on the basis of the procedures described in the par. 4.1 and have been optimized using a selected sample of MC events. For a

preliminary analysis, we selected a reduced DIS sample according to the following criteria:

- selection of the volume tracks with four consecutive basetracks on the first 4 plates downstream.
- basetracks with slopes smaller than 500 mrad
- basetracks with a high probability to satisfy the hypothesis that they belong to the same volume track ($eProb > 0.9$).

We obtained 1217 predictions of DIS events, starting from the first plate, out of 5000. This number is mainly due to the first requirement, taking account of the $\sim$78% simulated efficiency.

4.4 Scanback algorithm

The first algorithm performs a scanback procedure "offline" on the selected predictions to localize the interaction points. The parameters to follow the tracks on each plate of the brick, have been set in such way that the candidate basetracks with these requirements are read:

$$|S_L^c - S_L^p| \leq 0.03 + 0.05 \times \theta \quad mrad \tag{4.4}$$

$$|S_T^c - S_T^p| \leq 0.03 \quad mrad \tag{4.5}$$

$$|P_L^c - P_L^p| \leq 70 + 6 \times \theta \quad \mu m \tag{4.6}$$

$$|P_T^c - P_T^p| \leq 70 \quad \mu m \tag{4.7}$$

where c means candidate, p means predicted, S and P are the Slope and the Position of the tracks, L is the longitudinal coordinate and T is the transverse one. θ represents the angle between the basetrack and the z direction. In case of more than one candidate found the best one is selected according to the best angular agreement with the prediction. If no candidate are found the predictions are made in the next

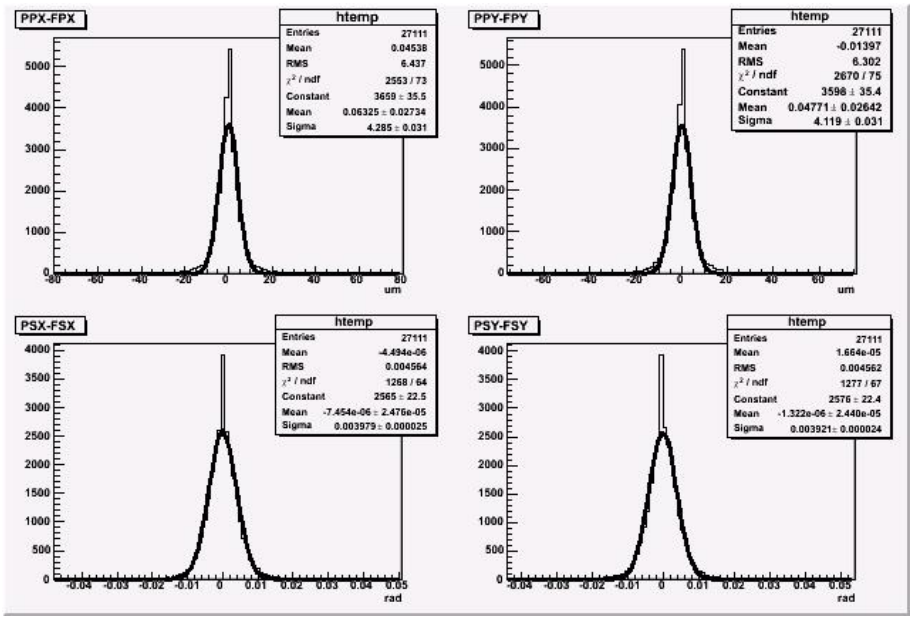

Fig. 4.7: Top (left-right):X-Y Position differences between the predicted and found tracks. Bottom (left-right): X-Y Angular differences between the predicted and found tracks.

plate and a new research is done with the same requirements. The algorithm repeats this procedure a maximum of three consecutive plates. At this point if the candidate is not found the track is declared *stopping*. The maximum number of allowed holes along the volume tracks is dependent on the basetracks efficiency. In our case, three consecutive holes provides a probability of fake stopping particles around 1.5% per plate. Fig. **??** shows the position and angular resolutions between the predicted and found basetracks for all plates. The position residuals are $\sim$4 μm. The angular residuals are $\sim$4 mrad. Both are compatible with the same resolutions obtained with the scanback online procedure on real data (see Donato). The distribution of the found tracks per plate is shown in fig. 4.8.

The output of this algorithm defines two track classes:

- stopping: tracks that after three consecutive holes are not followed any longer according to the criteria defined above.
- passing-through: tracks followed through the all data set. Note that in the

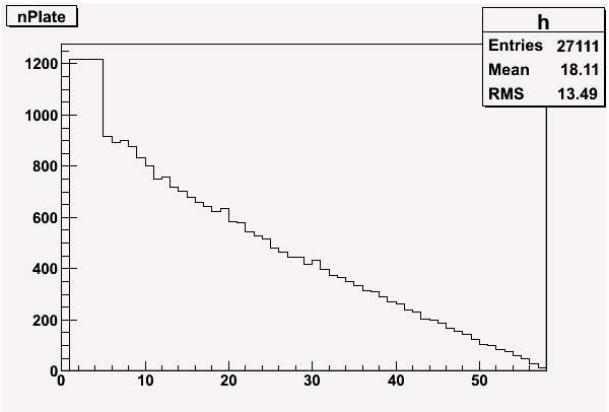

Fig. 4.8: Found tracks distribution versus plate ID

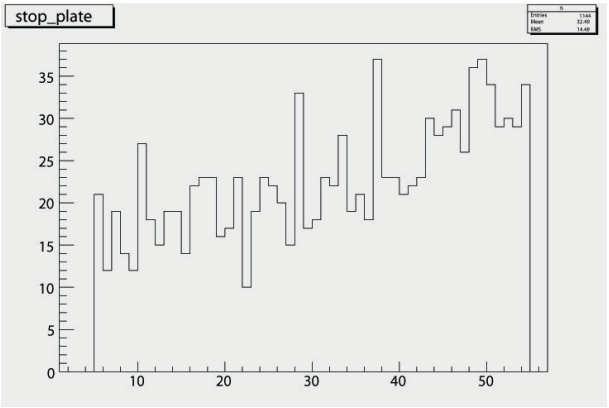

Fig. 4.9: Stopping point distribution for all plates

MC data only neutrino interactions are simulated but the tracks generated by neutrino interactions occurring in the first four plates are classified as *passing* by the scanback algorithm.

The found stopping points are 1147 as shown in fig. 4.9. We have also checked the tracking efficiency (∼78% from the simulation) on the Scanback (SB) passing-through tracks, as shown in fig. 4.10.

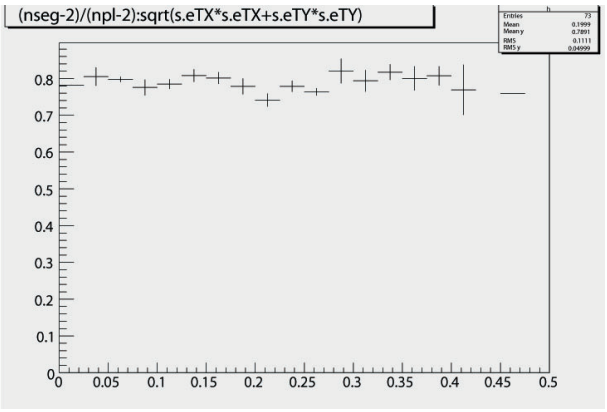

Fig. 4.10: Tracking efficiency on passing-through

4.5 TotalScan algorithm

The analysis on the real data would require a fine alignment among emulsion plates (already intercalibrated). Since we did not simulate any misalignment among plates we go to the further step. At this point, another algorithm opens around each stopping point a "virtual" volume filled with the basetracks segments in the aligned reference frame. The volume size has been chosen in order to get a high reconstruction efficiency without too much scanning time consuming. Taking as a reference "scanning" area 7×7 mm^2 since it includes a 400 mrad cone open from the neutrino vertex down to 5 plates downstream, the probability of reconstructing same multiplicity as 7x7 mm2 with an area 5×5 mm^2 is (97±1)%.On this basis, we set the volume scan size 5×5 mm^2 × 11 plates (5 upstream and 5 downstream the stopping point plate) and performed the TotalScan procedure on the 1147 stopping points. The result is that: 1057 MC events have been recognized out of 1147. This is due to the fact that in some volumes more than one followed scanback track has led to the same neutrino interaction.

935 neutrino interactions out of 1057 have been localized and confirmed by TotalScan in a range of three plates as shown in fig. 4.11, while the remaining 122 are not confirmed. The fig. 4.12 shows a summary of these preliminary results

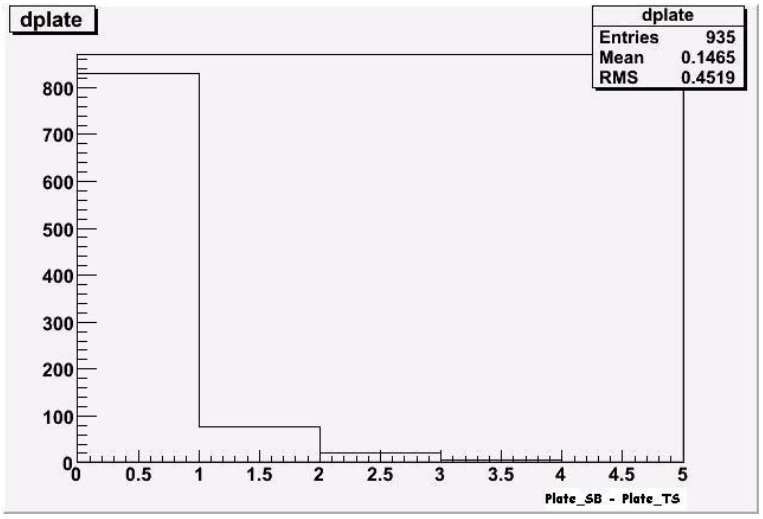

Fig. 4.11: Plate Differences between ScanBack and TotalScan plates. The stopping points are confirmed within 3 plates

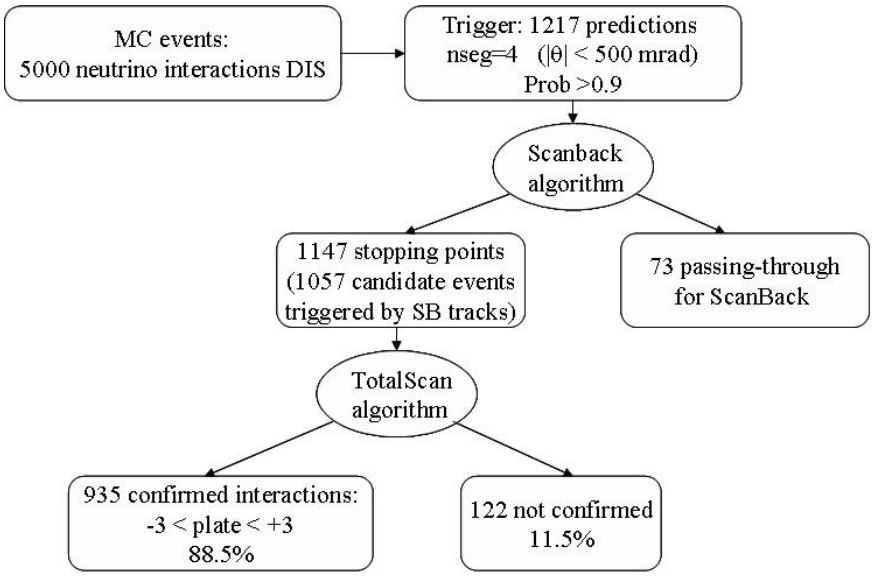

Fig. 4.12: Summary of the Scanback and Total Scan results

4.6 Vertex reconstruction

The vertex reconstruction algorithm is based on FEDRA tools.First, let us to consider the volumes containing the 935 confirmed interactions and apply the vertex reconstruction algorithm to identify neutrino events. The basetracks filling the volumes, will be linked together in order to build the volume tracks. Then we can perform the vertex reconstruction. For a preliminary analysis, on the basis of the estimated efficiency, we defined topological cuts on the vertex tracks with the following parameters:

$$\begin{array}{c} \Delta z < 4000 \quad \mu m \\ ImpactParameter(IP) < 50 \quad \mu m \end{array} \tag{4.8}$$

where Δz is the maximal longitudinal distance between tracks and founded vertex, and IP is the maximal 3D distance between tracks. The algorithm works taking account that we don't have any recognition of the particle identity and momentum P. A preliminary result shows that:

- 392 out 935 interactions are identified by the primary μ but the vertex is not reconstructed. This is due to the low tracking efficiency but also to the presence of tracks with a momentum too low. Tracks with P<0.5 GeV are not reconstructed by the algorithm.
- the remaining 543 are reconstructed as single-track and multi-track events.

The vertex reconstruction results are summerized in the fig. 4.13. Fig 4.15 shows the Δz distribution and the Impact parameter of the 543 reconstructed vertex. The distribution of the reconstructed multiplicity (see fig 4.16) for the same number of events is compared with that expected from MC truth for DIS(fig 4.17).

Fig. 4.18 shows the interaction products for MC Truth and for reconstructed vertex.

Going back to the TotalScan results, we have still to classify the 122 not confirmed interactions. They have been checked using both TotalScan and event reconstruction algorithms giving the following results:

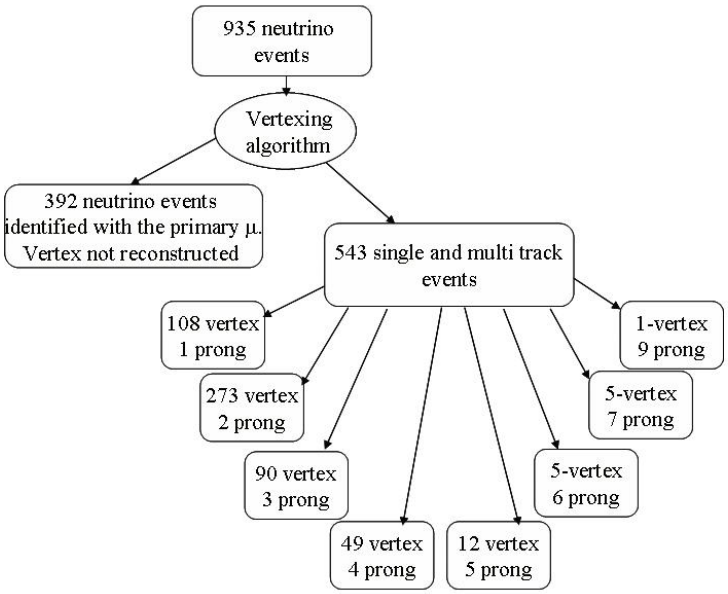

Fig. 4.13: Vertex reconstruction results

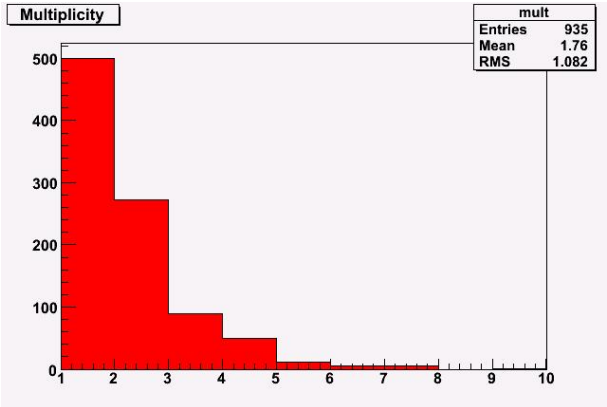

Fig. 4.14: Charged-particle multiplicity after event reconstruction.

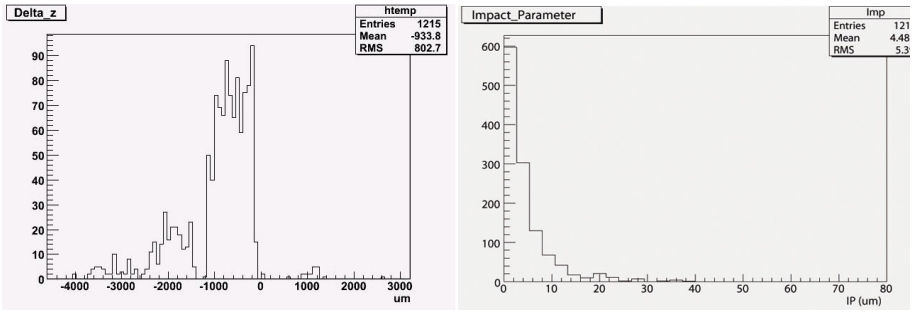

Fig. 4.15: Reconstructed vertex: track-vertex longitudinal distance distribution on the left side. impact parameter distribution on the right side

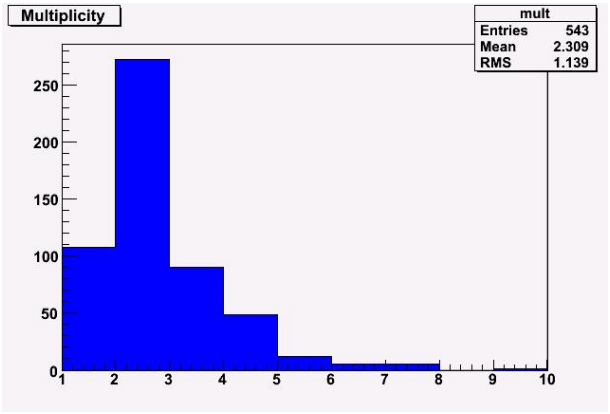

Fig. 4.16: Charged-particle multiplicity of the 543 single and multi-track events, after vertex reconstruction.

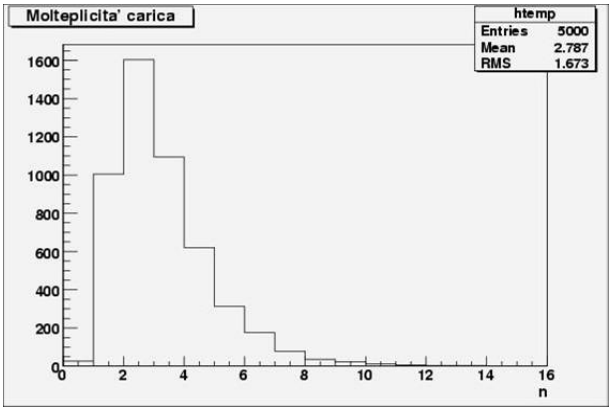

Fig. 4.17: MCTruth: Charged-particle multiplicity for DIS neutrino interactions.

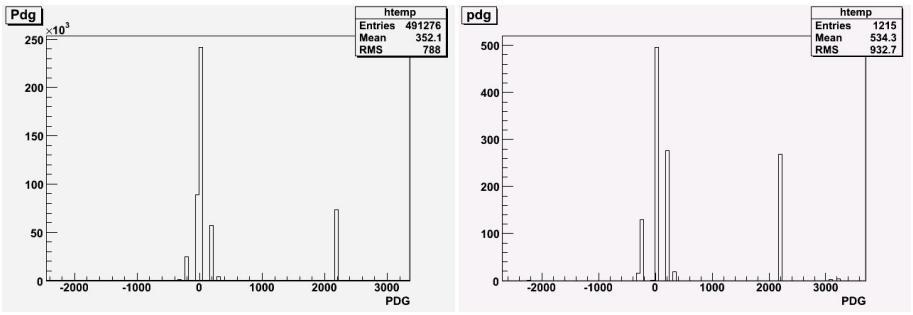

Fig. 4.18: MC Truth: Charged-particle multiplicity for DIS neutrino interactions.

- 43 out of 122 are classified passing-through by the algorithms. The neutrino interaction occurs several plates upstream the stopping plate.
- 40 are classified as fake stop, due mainly to the not high efficiency.
- 35 volumes where the ScanBack tracks are not reconstructed.
- 4 confirmed stop. These tracks are products of secondary interactions.

4.7 Background evaluation

In MC data the environmental background as well as the cosmic ray tracks has not been simulated. In order to provide a background estimation, as first attempt we have mixed 56 general scan measurements of the BL088 to the 5000 DIS neutrino interactions simulated. This is possible in a first approximation, beacause the signal to noise ratio is really in favour of the background. The number of neutrino interactions expected in this brick normalized to the scanning area (80 cm^2) is very small, around 97, so the probability to connect an MC simulated event to a real signal event basetrack is very low. We have considered this background as uncorrelated since we did not perform the alignment among plates. Only our simulated events are aligned. The next step is to perform the all procedure starting from the same sample of predicted seleted events: scanback until the volume analysis as done for the pure MC sample. The first results given from the ScanBack algorithms are:

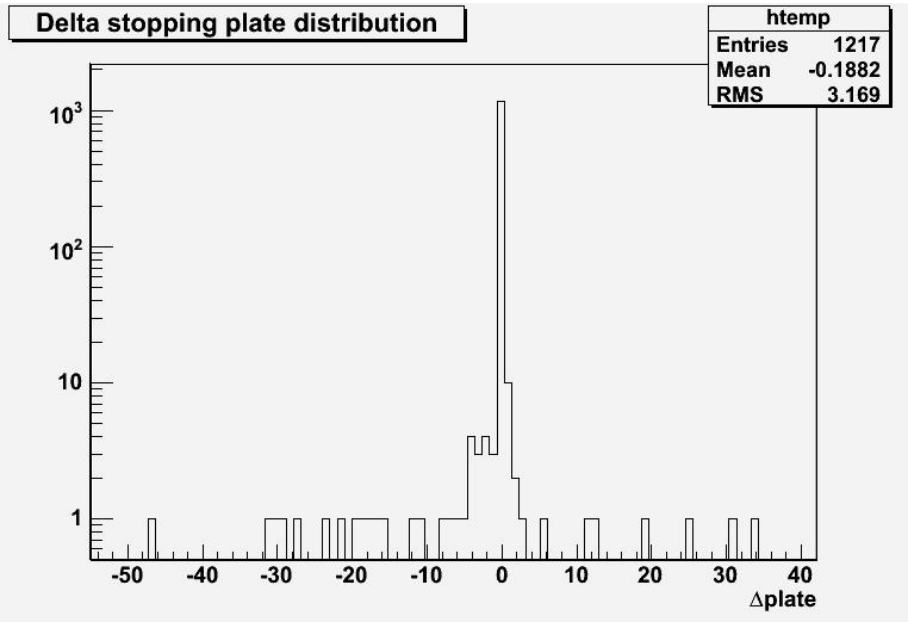

Fig. 4.19: Distribution of the differences between stopping plates for the pure MC events and for the events mixed to background

1121 out of 1217 are stopping points;

the remaining 93 are passing-through.

Fig. 4.19 shows the distribution of the differences between the stopping plate for the simulated events and for the same events mixed with the background. As we see, in both cases most tracks stop on the same plate within a range of 3 plates.

Also the found tracks distribution per plate for both cases are not significantly different as shown in fig. 4.20.

The background contribution does not affect the neutrino event reconstruction in a significant way. Only 52 tracks stop on different plates,(out of the range of 3 plates) due to the presence of background. In these cases a background basetrack has been wrongly connected to the MC signal track, loosing the possibility of reconstructing the neutrino event. We can estimate that the background contribution to this analysis is lower than 5%.

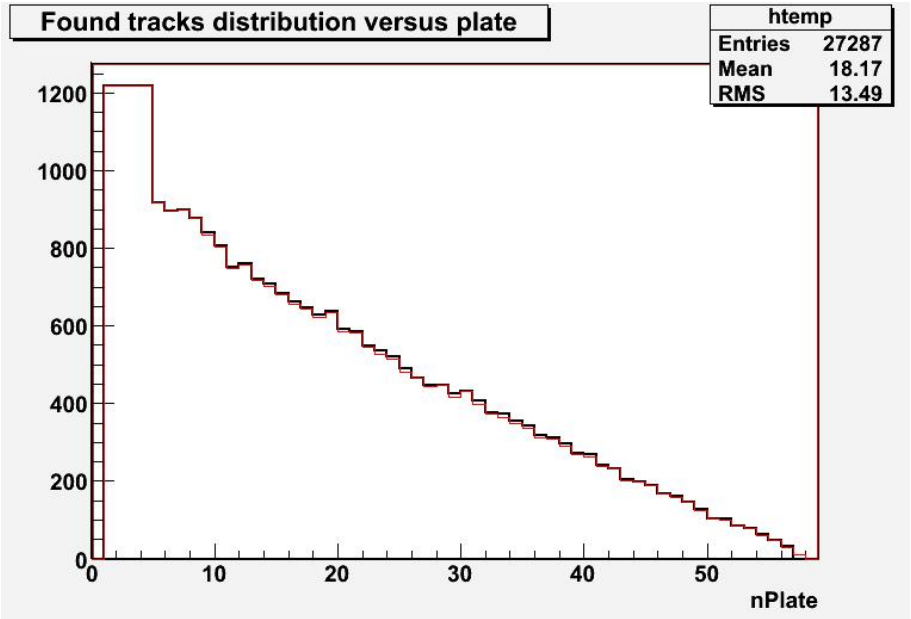

Fig. 4.20: Found tracks distribution versus plate for the pure simulated events (black line) and for the events + background (red line)

Conclusions

The OPERA experiment aims at the confirmation of $\nu_\mu \rightarrow \nu_\tau$ oscillations through the direct observation of τ neutrinos in an initially pure ν_μ beam. The large amount of nuclear emulsions used in OPERA , requires fast automatic scanning microscopes with high speed and accuracy.

This thesis work has contributed to the optimization of Bologna microscopes performances. The goal of 20 cm^2/hour scanning speed has been achieved. The tracking efficiency was measured to be 90% for minimum ionizating particles with an incident angle up to 500 mrad. The measured instrumental background, was reduced to the order of 2 tracks/cm^2.

The main contribution of this thesis concerns the development and study of the algorithms for the localization and reconstruction of the neutrino interactions in an OPERA brick. The performances of the algorithms have been optimized and estimated using Monte Carlo simulated data. The simulation concerned the experimental test PEANUT, made at Fermilab. In this test, a mini-detector, similar to OPERA, was exposed to the NuMI neutrino beam line. The algorithms perform the procedure adopted for OPERA emulsion analysis. The first algorithm implements an off-line ScanBack procedure : the tracks are followed plate per plate according to well defined tolerances in order to localize the interaction points. The TotalScan procedure creates "virtual volumes" of few squared millimiters per a given number of plates, around each stopping point, for the event classification. Another algorithm performs the event reconstruction in the volumes. We obtained a reconstruction efficiency of 89% on the selected Deep Inelastic Scattering events. The algorithms, optimized on the basis of the simulation, have been used on a real Peanut brick.

The number of reconstructed neutrino interactions in the analysed volume, after the MC efficiency correction, is in agreement with the number of events expected from the simulation.

Bibliography

[1] W. Pauli, letter to a physicist's gathering at Tubingen, December 4, 1930. Reprinted in *Wolfgang Pauli, Collected Scientific Papers*, ed. R. Kronig and V. Weisskopf, Vol. 2, p. 1313 (Interscience: New York, 1964).

[2] F. Reines and C.L. Cowan, Nature 178 (1956) 446.

[3] Danby et al, *Phys. Rev. Lett* 70 (1977) 487.

[4] ALEPH Coll., Decamp et al, Phys. Lett. B 235 (1990) 399.

[5] K. Kodama, et.al., Phys. Lett. B504 (2001) 218.

[6] S.L. Glashow, Nucl. Phys., 22 (1961) 579.

[7] S. Weinberg, Phys. Rev. Lett. 19 (1967) 1264.

[8] A. Salam, Proceedings of the 8th Nobel Symposium on Elementary particle theory, relativistic groups and analyticity, (1968), ed. Swartholm, Almquist and Wiksells, 367.

[9] T.J. Loredo et al., Phys. Rev. D65 (2002) 063002, 39 pp.

[10] C. Kraus et al., Eur. Phys. J. C40 (2005) 447.

[11] V.M. Lobashev et al., Phys. Lett. B460 (1999) 227.

[12] A. Osipowicz et al., hep-ex/0109033

[13] Assamagan et al., PhyRevD 53 (1996)6065

[14] Barate et al., Eur. Phys. J. C2 (1998)395

[15] C.L. bennett et al., astro-ph/0302207

[16] M. Colless et al., astro-ph/0306581

[17] D.N. Spergel et al., astro-ph/0302209

[18] S. Bilenky and S. Petcov, Rev. Mod. Phys. 59 (1987) 671; B. Kayser, Neutrino Mass, eds. G. Altarelli and K. Winter, Springer Tracts in Modern Physics (2003).

[19] H.V. Klapdor-Kleingrothaus et al., Eur. Phys. J. A12(2001)147

[20] H.V.Klapdor-Kleingrothaus et al.; Phys. Lett. B 586,198 (2004).

[21] R. Ardito et al., arXiv:hep-ex/0501010v1 6 Jan 2005

[22] S.Pirro et al., Nuclear Physics B - Proceedings Supplements Vol 138, January 2005, pp 210-213

[23] Double beta decays and solar neutrinos with ^{100}Mo -MOON(Mo Observatory Of Neutrinos) May 24,2005 v1.1

[24] B. Pontecorvo,Zh. Eksp. Theor. Fiz. 33, 549 (1957).

[25] The MACRO Collaboration, Matter Effects in Upward-Going Muons and Sterile Neutrino Oscillations, arXiv:hep-ex/0106049v2 14 June 2001.

[26] L. Wolfenstein, Phys. Rev. D 17 (1978) 2369. S. Mikheyev and A. Smirnov, Sov. J. Nucl. Phys. 42 (1986) 913; Sov. Phys. JETP 64 (1986) 4; Nuovo Cim. 9C (1986) 17.

[27] J. N. Bahcall et al., Astrophys. J. 555 (2001) 112001

[28] Cleveland, Bruce T. et al., Astrophys. J. 496 (1998) 505-526

[29] kamiokande Collaboration, Y. Fukuda et al., Phys. rev. Lett. (1996) 1683-1686

[30] SuperKamiokande Collaboration, S. Fukuda et al., Phys. Rev. Lett. 86 (2001) 5651.

[31] Gallex Collaboration, W. Hampel et al., Phys. Lett. B447 (1999) 127. GNO Collaboration, M. Altmann et al., Phys. Lett. B490 (2000) 16

[32] SAGE Collaboration, J.N. Abdurashitov et al., arXiv:astro-ph/0204245 v2 9 Jul 2002

[33] SNO Collaboration, S. Ahmed et al., Phys. Rev. Lett. 92(2004) 181301

[34] KamLand Collaboration, K. Eguchi et al., Phys. Rev. Lett. 90(2003) 021802; T. Araki et al., Phys. Rev. Lett. 94(2005) 081801

[35] Aglietta M. et al., Europhys. Lett. 15 (1991) 559-564

[36] Daum, K et al., Z. Phys. C 66 (1995) 417

[37] Kafka, T., proc. of Sixth International Workshop on Topics in Astroparticle and Underground Physics, Paris 1999.

[38] Casper, D. et al., Phys. Rev. Lett. 66 (1991) 2561; Becker-Sxendy, R. et al., Phys D 46 (1992) 3720

[39] Measurement of the flux and zenith angle distribution of upward through-going muons in Kamiokande II + III, Hatakeyama, S. et al. (Kamiokande), Phys. Rev. Lett. 81 (1998) 2016-2019

[40] Atmospheric neutrino results from SuperKamiokande, E. Kearns (Super-Kamiokande), 2004. Neutrino 2004, 13-19 June 2004, Paris, France; SuperK recent results, Scholberg, K. (Super-Kamiokande), 2005. 20th International Workshop on Weak Interactions and Neutrinos (WIN'05), June 6-11, 2005, Delphi, Greece

[41] W.W. Allison *et al.*, Phys. Lett. B449 (1999) 137; M. Sanchez *et al.*, Phys. Rev. D 68, 11304 (2003).

[42] The MACRO Collaboration (M.Ambrosio *et al.*), Eur. Phys. J. C 36, 323 (2004).

[43] G¿ Battistoni et al., Phys. Lett. B 615 (2005); G.L. Fogli et al., Phys. Rev. D 60 (1999) 053006.

[44] The CHOOZ Collaboration, Limit on Meutrino Oscillations from the CHOOZ Experiment arXiv:hep-ex/9907037 v1 19 Jul 1999

[45] The Palo Verde Collaboration, Results from the Palo Verde neutrino oscillation experiment, Phys. Rev. D, Vol62 072002 (2000)

[46] Ahn, K2K Collaboration, Measurement of neutrino oscillation by the K2K experiment Phys. Rev. D74 (2006)

[47] MINOS Collaboration, First MINOS results from the NuMI beam, arXiv:hep-ex/0605058 v2 23 May 2006.

[48] OPERA Collaboration, OPERA: An appearance experiment to search for $\nu_\mu \leftrightarrow \nu_\tau$ oscillations in the CNGS beam. Experimental proposal, CERN-SPSC-2000-028 (2000); OPERA Collaboration, Status report on the OPERA experiment, CERN/SPSC 2001-025 (2001); http://operaweb.web.cern.ch/operaweb/index.shtml.

[49] Observation of Tau Neutrino Interactions by DONUT collaboration (Dec 14 2000); http://arxiv.org/ftp/hep-ex/papers/0012/0012035.pdf

[50] G. Acquistapace *et al.*, CERN 98-02, AE-98/05, (1998).

[51] The OPERA Collaboration, First Events from the CNGS neutrino beam detected in the OPERA experiment, New Journal of Physics * (2006) 303.

[52] A.E. Ball et al., CERN-EP-2001-017 (2001).

[53] E. Barbuto et al., Nucl. Instr. Meth. **A 525** 485 (2004).

[54] M. Komatsu, P. Migliozzi and F. Terranova, J. Phys. G **29** 443 (2003).

[55] G.P.S. Occhialini, C.F.Powell, Nuclear Disintegraions Produced By Slow Charged Particle of Small mass, Nature **159**, 186-190, **160**, 453-456 (1947).

[56] Ushida et al., Phys. Rev. Lett., (1981) 47,24

[57] CHORUS collaboration, NIM ,A 401 (1997), 7-44.

[58] C. Sirignano, *R&D* on OPERA ECC: studies on emulsion handling and event reconstruction techniques.

[59] W.J. Smith, Modern optical engineering, the design of optical systems, Third Edition, McGraw-Hill (2000).

[60] D. Di Ferdinando, Experimental study of neutrino interactions in the OPERA-like ECC, Ch 5